CHAPTER 6:

INVESTIGATION OF PLANE STRAIN AND AXISYMMETRY

6.1 Introduction

The purpose of the finite element parametric study, undertaken in Chapters 7 - 10, is to investigate the reinforcement mechanisms operating in a two-layer soil system, with and without the inclusion of a membrane possessing a medium angle of friction ($\phi_i = 35°$), and the influence upon those mechanisms of certain material properties. The effects upon the performance of the two-layer soil system of including a low friction membrane ($\phi_i = 10°$) are investigated in Chapter 11. The key areas of investigation are, (a) the load-displacement responses, (b) the stresses acting at the fill-clay, or fill-reinforcement-clay, interfaces and (c) the reinforcement tensions.

The important material properties of a two-layer soil system, which are varied in the parametric study, are the thickness and strength of the fill layer (Chapter 7), the reinforcement stiffness (Chapter 8), the reinforcement length (Chapter 9) and the clay shear strength (Chapter 10). The majority of these parametric studies are conducted for plane strain conditions only, with the notable exception of the investigation of the influence of the clay strength (Chapter 10) which is for plane strain and axisymmetry. To conduct a thorough parametric investigation it is first necessary to establish the most appropriate numerical approach. These preliminary plane strain studies are described in Sections 6.2 and 6.3.

Utilising the optimum numerical approach established in the first part of this chapter, Section 6.4 proceeds to compare the results of the three key areas for a plane strain and a corresponding axisymmetric analysis for the unreinforced and reinforced case, using the newly developed elements from Chapters 4 and 5. A detailed investigation of the displacements, strains, stress distributions, principal stress directions in the fill, the mobilised friction angle and the stress distributions on the underside of the footing, for the plane strain and axisymmetric reinforced and unreinforced 'central parametric analyses' is undertaken in Section 6.5.

6.2 Specification of the Parametric Study

The philosophy that is adopted throughout this study is to investigate thoroughly the properties of a two-layer soil system by examining the monotonic load behaviour of a reinforced and unreinforced structure. The influence and effects of certain specific reinforcement and soil parameters are then studied carefully by varying those parameters and conducting investigations of the three key areas listed earlier.

The parametric study of two-layer soil systems is conducted with particular consideration for their practical application as reinforced and unreinforced unpaved roads, since this is the most researched use of two-layer soil systems, but the study is also very relevant to all other uses of such structures. The study is accomplished by considering a 'typical two-layer soil system', schematically shown in Figure 6.1, as a central analysis, which is allocated both a specific geometry and a set of typical material properties, which are varied individually.

The central analysis of the 'typical two-layer soil system' is established by considering the conventional design of unpaved roads and the characteristic properties of the reinforcement, the aggregate subbase and clay subgrade usually found at the sites of unpaved reinforced roads, as well as the average wheel widths of the lorries used to traffic such roads. These central analysis parameters are all given in Appendix 6A. The soil properties are intended to be representative of a typical reinforced unpaved road built on a clay subgrade of medium strength, therefore an undrained shear strength of $s_u^{PS} = 30\ kPa$ (plane strain) is

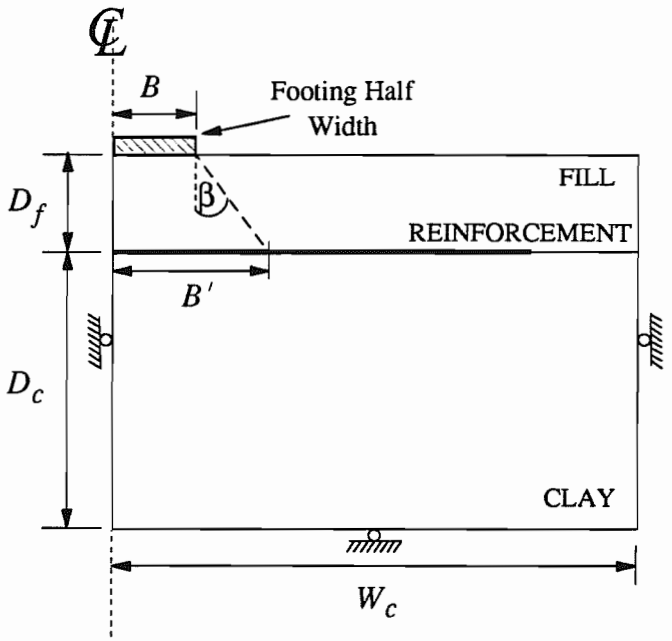

Figure 6.1: The 'Typical Two-Layer Soil System'

chosen, which is classified as 'soft' in British Standard CP 2004 (1972). The aggregate fill generally used for unpaved roads is a Type 1, or occasionally Type 2, Subbase Material (see Specification for Highway Works (1986)), which has a mean peak friction angle of between $\phi_{peak} = 46° \rightarrow 56°$, and it is frequently laid at an average depth of around $D_f = 300\ mm$ ($\pm 100\ mm$) for such applications as on-site haul roads. Geosynthetic reinforcements are manufactured with a wide range of material stiffnesses (in the order of between $J = 30 \rightarrow 2000\ kN/m$ approximately), but a proprietary polymeric geogrid material would typically have a stiffness of $300\ kN/m$. Finally, from investigations of previous unpaved road trials, (e.g. the full-scale reinforced haul road test at the Science and Engineering Research Council owned Soft Clay Site at Bothkennar, Little (1992), and the Transport and Road Research Laboratory tests, Pike *et al.* (1977)), the typical overall width of the double-tyred wheel on the lorries used, is found to vary only slightly from between $0.51\ m \rightarrow 0.47\ m$. Therefore a wheel (or footing) width of $0.5\ m = 2B$, with a perfectly rough contact, is adopted throughout this research. Although there are, obviously, two sets of double-tyred wheels, one at each end of the lorry axle, they are usually sufficiently widely spaced so that they may be regarded as independent footings for design purposes. It is also

worth noting that although the wheels are generally double-tyred (as shown in Figure 1.1), the loading is considered as a single wheel load since the separation of the tyres is effectively negligible.

The finite element analyses are all displacement controlled so that a constant final vertical footing displacement of $\delta = 0.15\ m = 0.6\ B$ is obtained in each finite element run. At this vertical displacement the associated rut that would develop in an unpaved road is generally considered to be too deep for the minimum clearance required by the majority of lorry traffic. If trafficking becomes impossible then the unpaved road has effectively failed, therefore the footing pressure required to achieve this displacement will be considered as the ultimate (or final) footing pressure P_f, for that particular road.

Since the unpaved road is symmetrical, it is only necessary to consider the half of the problem about a centre-line through the footing load, provided that appropriate constraints are employed along the finite element mesh centre-line, as shown in Figure 6.1. That is, fixity in the horizontal 'x' direction and freedom in the vertical 'y' direction, i.e. a roller type boundary.

6.3 Experiments with Preliminary Plane Strain Meshes

To run a finite element parametric study it is essential to use a mesh of an appropriate size with an element density that is optimum, in terms of computational efficiency and numerical accuracy, which is discussed in Sections 6.3.1 and 6.3.2 respectively. The influence of the mesh boundaries is assessed in Section 6.3.3, and Section 6.3.4 investigates the differences in calculated behaviour between a large and small displacement analysis. The various reinforcement mechanisms acting at large and small displacements are identified in Section 6.3.5.

6.3.1 Mesh Size

Initially it was assumed that the size of the finite element mesh needs to be only sufficiently large to contain the size of the clay plasticity zones as predicted by plasticity theory,

illustrated in Figure 6.2. A similar assumption was made by Poran (1985). The load distribution through the fill is simplified to a uniform pyramidal distribution given by a constant load spread angle, β, as described in Section 6.3.5.

Giroud and Noiray (1981) suggested that, according to the theory of plasticity (as explained in Calladine (1985) and Bolton (1979)), the overall width of the plastic failure zone (W_P shown in Figure 6.2) in a frictionless incompressible subgrade underlying a geotextile reinforced subbase is:-

$$W_P = 3\,(2B + 2D_f \tan\beta) \tag{6.1}$$

where B , D_f and β are the same as illustrated in Figure 6.1.

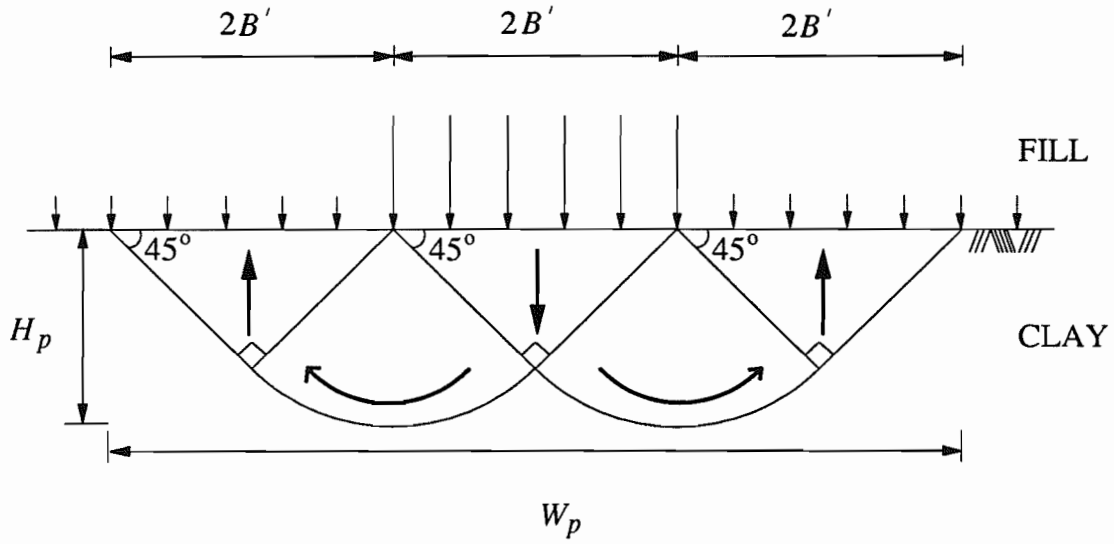

Figure 6.2: Plastic Failure Mechanism in Cohesive Material (After Bolton (1979))

This width (W_P) serves as a guide-line for the required width of the finite element mesh. The minimum depth of the plastic failure zone in the clay (H_P shown in Figure 6.2), is:-

$$H_P = (B + D_f \tan\beta)\sqrt{2} \tag{6.2}$$

Similarly, this depth serves as a guide-line for the minimum required depth of the clay. The overall minimum depth of the mesh is the sum of the thicknesses of the subbase and the clay (i.e. $D_f + H_P$).

From approximate and exact load distributions given by Perloff and Baron (1976) it is suggested that a load spread angle, such as β in Figure 6.1, should be taken as $\beta = \tan^{-1} 0.5 \approx 26.6°$. However, Taylor (1965) suggests that a load spread angle of $30°$ is still conservative. Poran (1985) estimated from plate bearing test results and from the finite element analyses of those tests, that an angle of the order of $45°$ was appropriate. A comprehensive list of the recommended load spread angles by other authors is presented in Craig and Chua (1990). From the plane strain finite element results of this dissertation it is estimated, by the method described in Section 6.3.5, to be an average value of about $40°$ for the particular material properties chosen (Appendix 6A). Using $\beta = 40°$, $B = 0.25\ m$ and $D_f = 0.3\ m$ in equations (6.1) and (6.2), the respective values of W_P and H_P are determined and hence the minimum required mesh size:-

$$\text{The minimum mesh depth} = D_f + H_P = 1.2B + 2.84B = 4.04B$$

$$\text{The minimum mesh } \textit{half} \text{ width} = W_P / 2 = 6.0B$$

At the base of the mesh it is felt that the boundary should be removed just beyond the minimum clay depth (H_P), in order to allay the amount of disturbance that any edge effects may cause to the predicted plastic zone. Therefore, the overall depth of the mesh is $D_f + D_c = 1.2B + 3.2B = 4.4B$. Additionally, a roller type boundary is used at the base similar to Burd (1986), rather than complete fixity as used by both Poran (1985) and Zeevaert (1980), since it is felt that there may still be some significant horizontal and shear stresses present. Although this introduces an artificial plane of weakness, it is considered sufficiently removed so as not to effect the results. It is assumed that another roller boundary condition at the minimum mesh half width distance of ($W_P / 2$) from the centre-line, is remote enough to prevent horizontal and shear stress concentrations occurring. As discussed in Section 6.2 the problem is symmetrical about the footing centre-line.

For comparison the finite element mesh sizes employed in other studies of two-layer soil systems, related to the relevant footing half widths (or radii), B , used in that study, are:-

Zeevaert (1980): $W_c = 6.0\,B$ and $D_c = 4.5\,B$ for $D_f = 1.5\,B$, $2.33\,B$

Griffiths (1982): $W_c = 9.2\,B$ and $D_c = 3.2\,B$ for $D_f = 0.8\,B$

Poran (1985): $W_c = 6.75\,D_f$ and $D_c = 4.5\,D_f$ for $D_f = 0.4\,B$, $1.0\,B$, $2.0\,B$

Burd (1986): $W_c = 13.33\,B$ and $D_c = 10.66\,B$ for $D_f = 1.33\,B$, $2.0\,B$, $2.67\,B$

Herein: $W_c = 6.0\,B$ and $D_c = 3.2\,B$ for $D_f = 0.6\,B$, $1.2\,B$, $2.0\,B$

The research conducted herein to examine the influence of the fill depth (Chapter 7) adopts the same philosophy as used by Zeevaert (1980) and Burd (1986), in that one constant set of dimensions are used for the size of the clay part of the mesh and for the footing width, while the fill depth is varied. Poran (1985) however, kept all the soil dimensions constant and varied the footing widths.

Using this mesh a series of plane strain finite element investigations are undertaken to determine the effects of element density and the mesh boundaries.

6.3.2 Mesh Density

The finite element method of analysis hinges on the process of being able to subdivide the entire problem into a finite number of representative components, or discrete parts, whose behaviour is readily understood. By 'rebuilding' the original system from these elements the behaviour of the whole system can then be studied. However, there are certain approximations and idealizations adopted for each element, which consequently cause slight inexact estimations. These discretization errors and other inherent inaccuracies, such as round-off, may prevent the calculation from converging to the correct result. It is generally accepted (Zienkiewicz (1977)) that the numerical approximation can be systematically improved to approach the exact answer by decreasing the size of the elements and hence increasing the total number of parameters specified at nodes.

The amount of distortion experienced by the elements during the large strain calculation can also have a detrimental influence on the accuracy of the numerical solution. Burd (1986) suggests that this difficulty may be dealt with either by refining the mesh in the region of

distortion, or by using a higher order quadrature rule for those elements that tend to become heavily deformed. Although Burd (1986) recommends the latter approach, the following investigative study adopts the former suggestion of improved refinement to try and alleviate numerical inaccuracies caused by unfavourable distortion effects, notice the large number of elements at the footing edge in Figure 6.3.

The consequences of varying the element sizes are investigated experimentally using the original mesh geometry established in Section 6.3.1 and a constant topography of element zones within the mesh. By maintaining a consistent mesh geometry, but increasing the total number of elements in the mesh, the density of elements increases and therefore the element sizes decrease.

The plane strain meshes for the four different numbers of elements (105, 240, 415 and 1000 elements) are shown in Figure 6.3. Each of the four finite element meshes, created using the mesh generator program OXMESH (Houlsby (1988)), are prescribed exactly the same material properties for the fill, clay and reinforcement, and subjected to the same final footing displacement of $0.6\,B$ in similar increment numbers (either 150 or 210 steps). This particular set of finite element analyses pre-dates the development of the plane strain interface elements.

The intention is to conduct a convergence study of the large displacement plane strain finite element results obtained for an increasing number of mesh elements and to effectively undertake a sensitivity study of how much these results are influenced by increasing the mesh resolution from 'coarse', Mesh P1, to 'fine', Mesh P4. The comparisons of the results (i.e. the load-displacement responses, the calculated stresses acting on the reinforcement and the reinforcement tensions at the footing centre-line) obtained for each mesh size are made with respect to the results of Mesh P4, since it is assumed that these results will be the closest to the exact answer given the practical constraints of computing time.

The pressure-displacement responses for each of the three coarser meshes (Mesh P1, P2 and P3) are compared to the response of Mesh P4 at each increment of footing displacement. Since the finite element calculations are done in either 150, or 210 increments of footing displacement, a linear interpolation is needed to establish values of footing

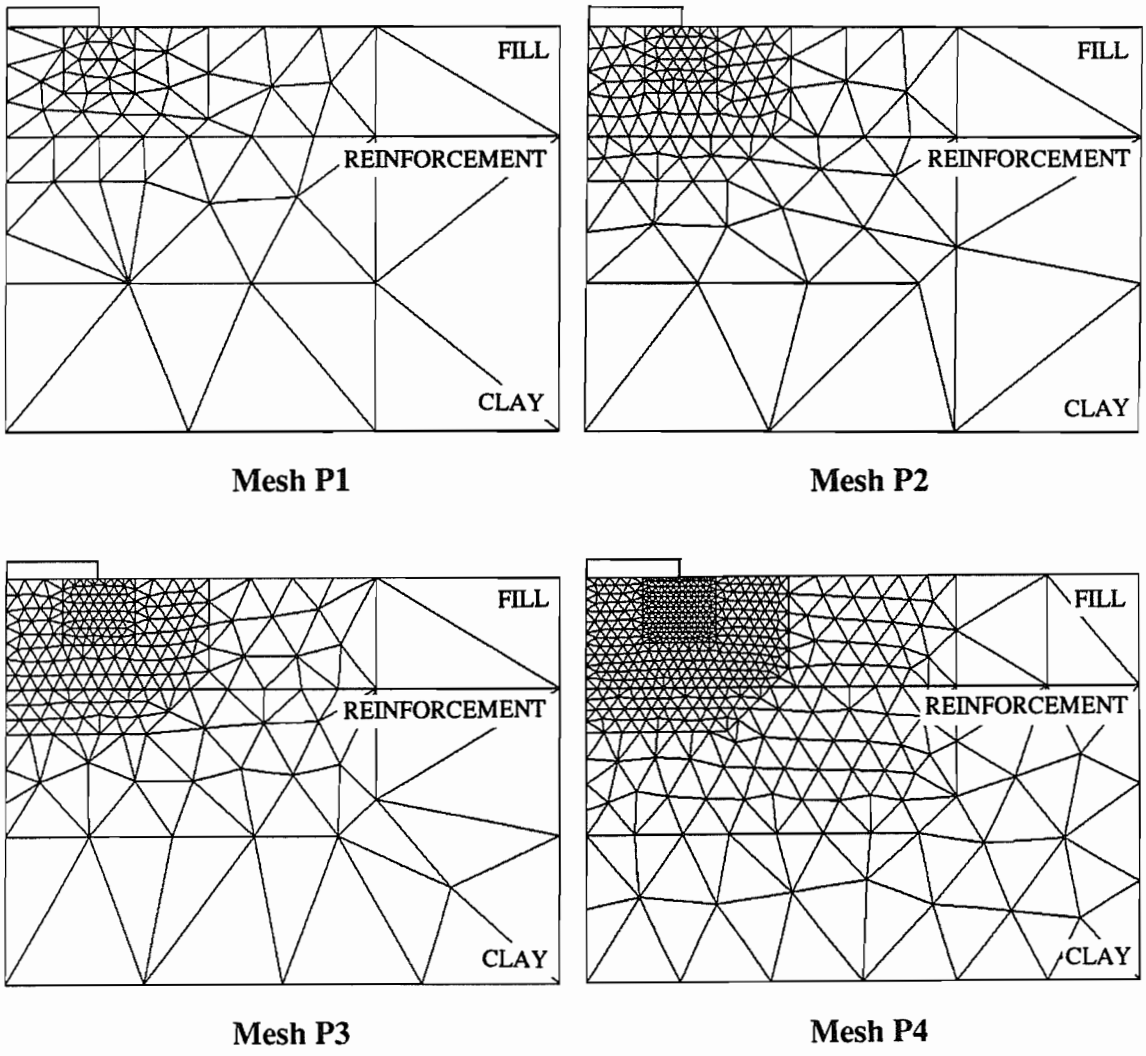

Figure 6.3: Four Finite Element Meshes with Varying Element Densities

pressure, from the Mesh P4 response, at all the various values of displacement used in the other three meshes. A total of the absolute percentage difference between each value of footing pressure for each run, compared to Mesh P4, is determined and averaged across the number of data. This, then, gives an average percentage error of the pressure-displacement response for each of the three coarser meshes in comparison to Mesh P4. These calculations of error are plotted in Figure 6.4.

The distribution of both shear and normal stress, above and below the reinforcement length, is calculated by Method 4 as described in Section 5.2. The absolute areas contained beneath these stress profiles for the coarser meshes are compared to the areas under the Mesh P4 stress profiles. The areas under the normal stress profiles are equal to the normal forces acting at the fill base and clay surface, while the areas under the shear stress profiles are equal to the shear forces exerted by the clay and the fill on the reinforcement. The percentage difference in these forces for each coarse mesh, with respect to Mesh P4, is also shown in Figure 6.4.

A distribution of the reinforcement tension along the reinforcement length is obtained by calculating the average of the three Gauss point stresses, per plane strain membrane element, plotted at the average distance of those Gauss points from the footing centre-line. The average value of stress is used because of the minor oscillations that occur in the tension distribution when each individual Gauss point stress is plotted. The reinforcement tension at the centre-line is deduced by linear interpolation from the averaged values of the tension for the first two membrane elements. The percentage differences in the centre-line tension, for each mesh with respect to Mesh P4, are shown in Figure 6.4.

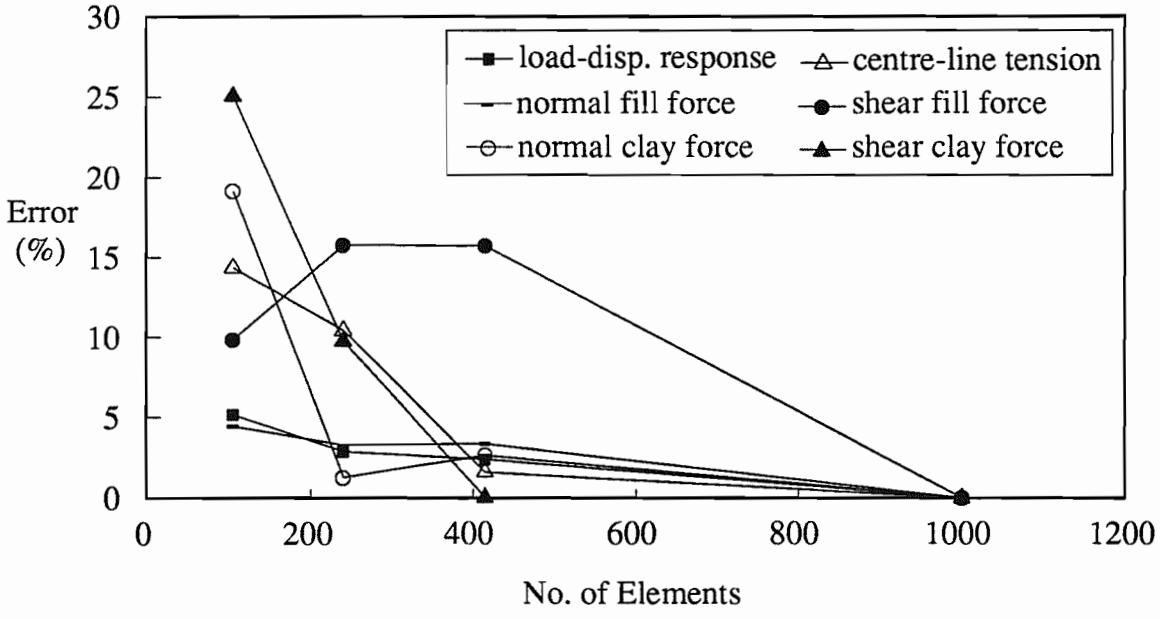

Figure 6.4: Percentage Error with Respect to Mesh P4 of the Finite Element Results

Figure 6.4 shows a series of six lines representing the percentage difference between the results obtained with Meshes P1, P2 and P3 compared to those obtained with Mesh P4. The assumption is made that any inherent error in the results provided by Mesh P4 is of an insignificant amount, implying that the percentage difference between the coarser meshes and Mesh P4 is an indication of the percentage error associated with those larger element sized meshes. The noticeably different trend of the shear fill force line, compared to the other five lines in Figure 6.4, is due to the spuriously low value of error estimated for Mesh P1 and the unexpectedly high value estimated for Mesh P3.

For Mesh P1 the errors vary considerably in each of the different calculations, with a maximum error of 25.1% obtained in the calculation of the shear force on the clay. Clearly, there are significant errors that develop in a finite element analysis which uses such a 'coarse' mesh.

For Mesh P2 the maximum error is obtained in the calculation of the shear force at the fill base, 15.8%. Although errors are also found in the estimations of the shear force at the clay surface and the reinforcement tension at the centre-line, approximately 10%. However, very small errors occurred in the prediction of the two normal forces and the load-displacement response, around 1.3% $\rightarrow$ 3.3%.

For Mesh P3 the majority of the errors are within just 3.4%, except for the shear force at the fill base which is 15.7% different from the shear force calculated using Mesh P4.

With regards to minimising any discretization errors and achieving a good approximation to the exact solution, then clearly the mesh to use would be Mesh P4. However, this fine mesh requires great amounts of computing time, which renders it almost useless as a practical design tool. Mesh P3, although less than half the number of elements compared to the fine mesh, still needed around 60% of the same computing time, and additionally had an average inherent error of about 4%. Therefore, it is decided that the optimum mesh size is Mesh P2, since this gives answers with an average percentage error of about 7%, but requires only 20% of the computing time compared to the fine Mesh P4. This error is considered as acceptable, unlike that for Mesh P1 which has an average

percentage error of 13% while still requiring 12% of the Mesh P4 computing time. Thus, for accuracy and efficiency Mesh P2 is used for the initial finite element calculations that are made with the mesh of clay dimensions $6B$ X $3.2B$.

6.3.3 Influence of Mesh Boundaries

The influence of the proximity of the mesh boundaries to the footing, on the results obtained from a plane strain large displacement finite element analysis, are investigated in this section.

The mesh dimensions for the clay part of the two-layer soil system were initially established in Section 6.3.1 as $W_c = W_P / 2 = 6B$ and $D_c = 3.2B$. However, a comparative analysis is conducted using a plane strain mesh with the clay dimensions of $W_c = 20B$ and $D_c = 20B$, and a fill thickness $D_f = 1.2B$ (illustrated in Figure 5.2), for the same two-layer soil system material properties given in Appendix 6A. This larger mesh is developed from the 240-element Mesh P2, shown in Figure 6.3, by increasing the area of the outer zone and adding in more elements, but maintaining the same element aspect ratio. Consequently the total number of triangular continuum elements increases from 240 (with 515 nodes) to 449 (with 1036 nodes). The $6B$ x $3.2B$ mesh was generated before the implementation of the plane strain interface elements, whereas the $20B$ x $20B$ mesh does possess interface elements at the fill-reinforcement and clay-reinforcement boundaries (as do all the other analyses reported in this chapter).

The results show that the clay subgrade actually yields outside of the theoretically predicted failure zones, such that the real failure depths are $H_P = 6.5B$ and $8.6B$ for the unreinforced and reinforced cases respectively (as opposed to $2.84B$) and the real failure half widths are $W_P / 2 = 4.4B$ and $6.3B$ (as opposed to $6.0B$). The true failure zone is clearly seen in Figure 6.5, which plots all the yielded Gauss points throughout the two-layer soil system at the final footing displacement $\delta = 0.6B$. The original mesh size is shown in Figure 6.5 to be well within the clay failure zone, particularly for the reinforced case, which demonstrates the need to select the mesh dimensions carefully.

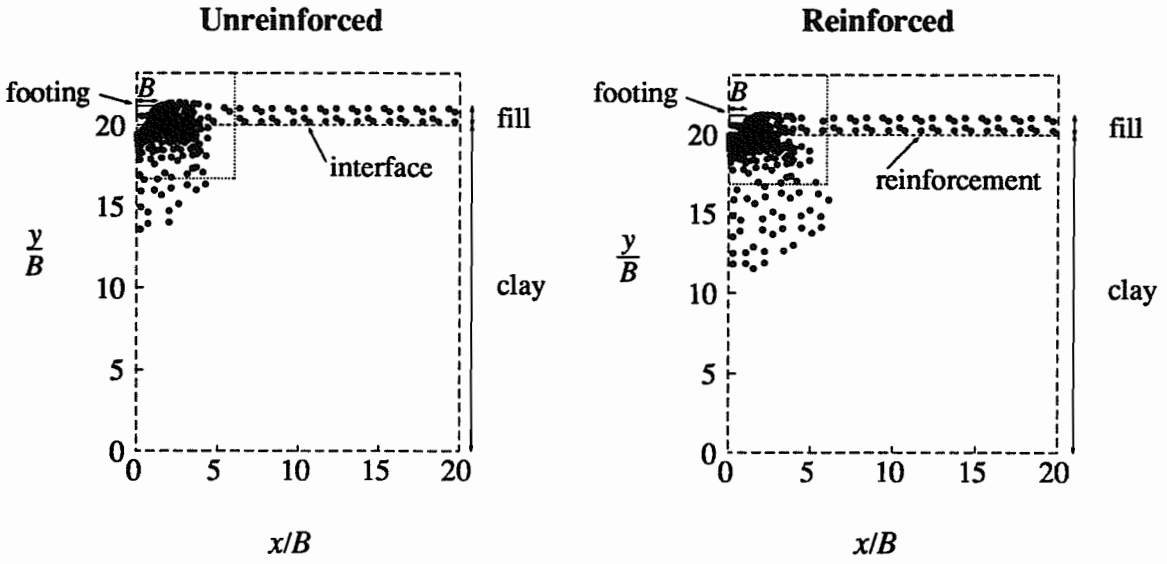

Figure 6.5: Yielded Gauss Points for the $20B$ X $20B$ Mesh B at $\delta = 0.6B$

Note that the horizontal, vertical and shear stresses that the fill layer experiences are sufficient to cause yield throughout its length in these particular plane strain analyses. This is discussed in more detail in Section 6.5.6.

Some of the consequences of using a larger mesh are that the initial elastic domain of the reinforced load-displacement response is approximately half as stiff as that for the smaller mesh and that the ultimate footing pressure, P_f, at a final displacement of $\delta = 0.6B$ is about 25% greater, as shown in Figure 6.6, where P / s_u^{PS} is the average value of vertical stress beneath the footing and δ / B is the vertical footing displacement.

Additionally, the normal stresses, σ, acting directly under the footing on the upper and lower reinforcement surfaces, Figure 6.7, are larger for the $20B$ X $20B$ mesh (extracted directly from the interface elements) than for the $6B$ X $3.2B$ mesh (obtained by Method 4, Section 5.2). At the centre-line ($x = 0$) the normal stresses are approximately 43% greater for the larger mesh compared to the smaller one. However as x increases the difference between these normal stresses reduces, such that at $x = 5B$ the difference in the estimated applied forces on the upper reinforcement surface (i.e. the areas under the upper normal stress curves between $x = 0 \rightarrow 5B$) is 8.6%, and similarly for the forces on the lower surface the difference is 11.1%.

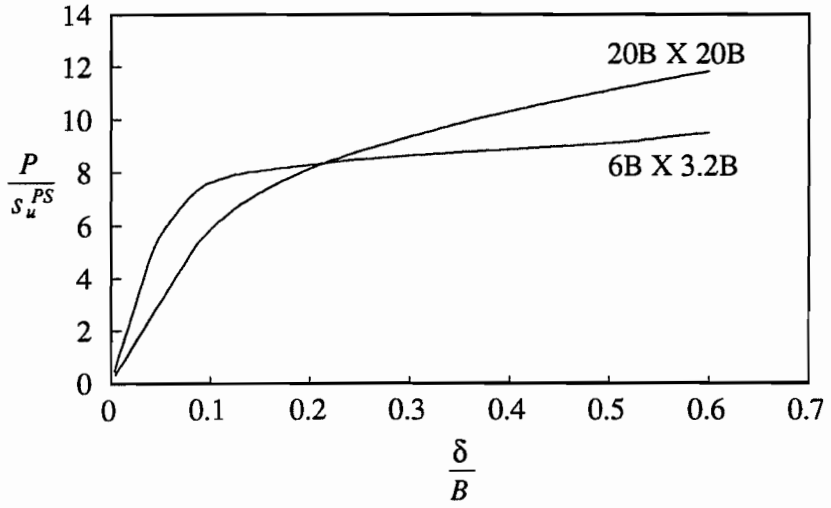

Figure 6.6: Pressure-Displacement Response for the Two Mesh Sizes ($20B$ X $20B$ and $6B$ X $3.2B$), using the same Material Properties

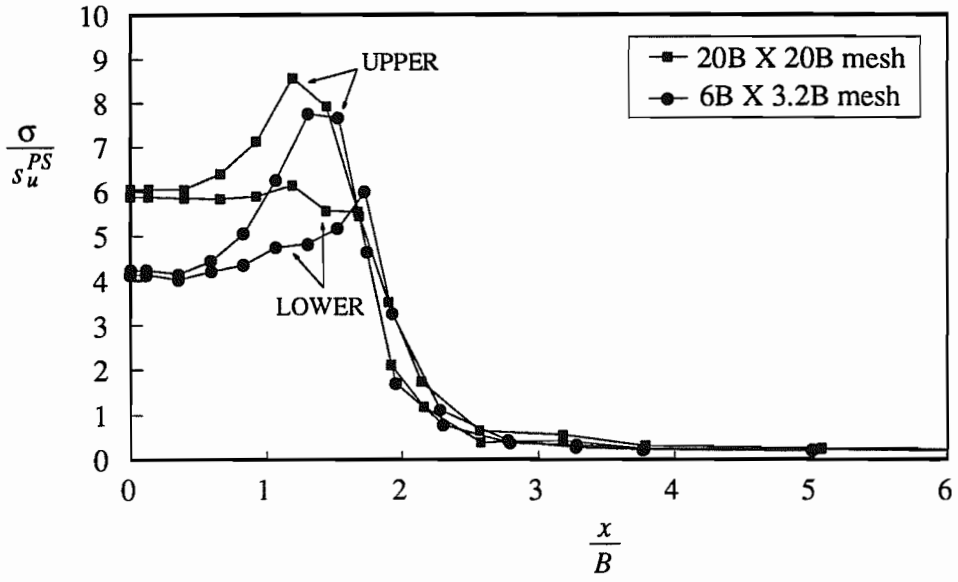

Figure 6.7: Normal Stresses (σ / s_u^{PS}) on Upper and Lower Reinforcement Surfaces for the Two Mesh Sizes, using the same Material Properties

Although there are quite considerable differences in the normal stress distributions for the large and small meshes, there is less of a difference between the reinforced shear stress

distributions, τ, Figure 6.8. The upper shear stress profiles follow an almost identical pattern, whereas the lower shear stress profiles do vary slightly, especially directly under the footing where the small mesh tends to over-predict the magnitude of the stresses.

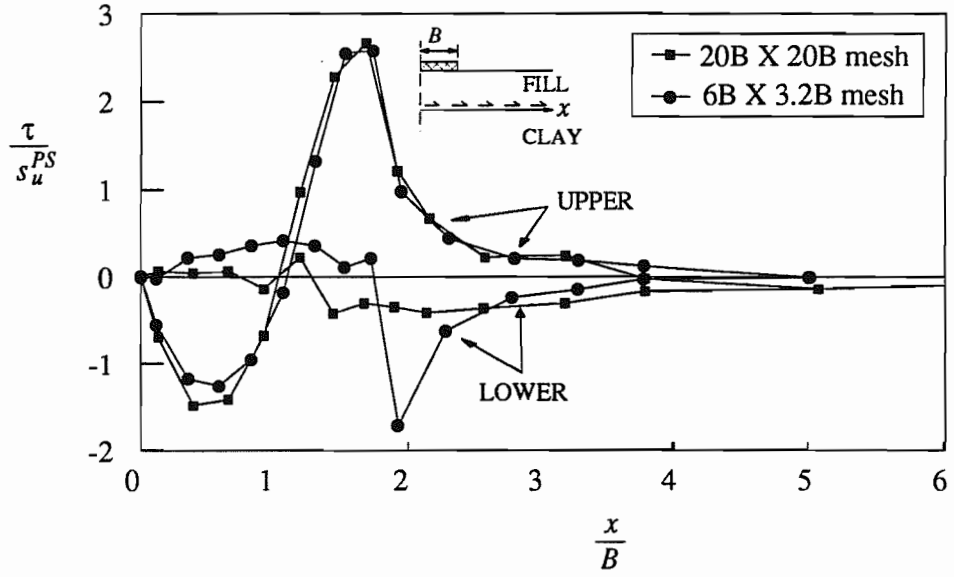

Figure 6.8: Shear Stresses (τ / s_u^{PS}) on Upper and Lower Reinforcement Surfaces for the Two Mesh Sizes, using the same Material Properties

The tension, F_r, along the length of the reinforcement, x, is shown in Figure 6.9. The larger mesh predicts a reinforcement tension at the centre-line which is 20% greater than the smaller mesh prediction.

Clearly the proximity of the two smooth boundaries to the footing have a considerable effect on the finite element results obtained. It is thought that the 20*B* X 20*B* mesh is likely to be larger than necessary, since an optimum mesh of $W_c = 10\,B$ and $D_c = 12\,B$, for the particular fill depth of $D_f = 1.2\,B$, should be sufficient to contain the real failure zone within the clay. Nevertheless, the parametric study is undertaken with a mesh of clay dimensions 20*B* X 20*B*, so that the solutions produced by the finite element analysis can be considered reliable and precise.

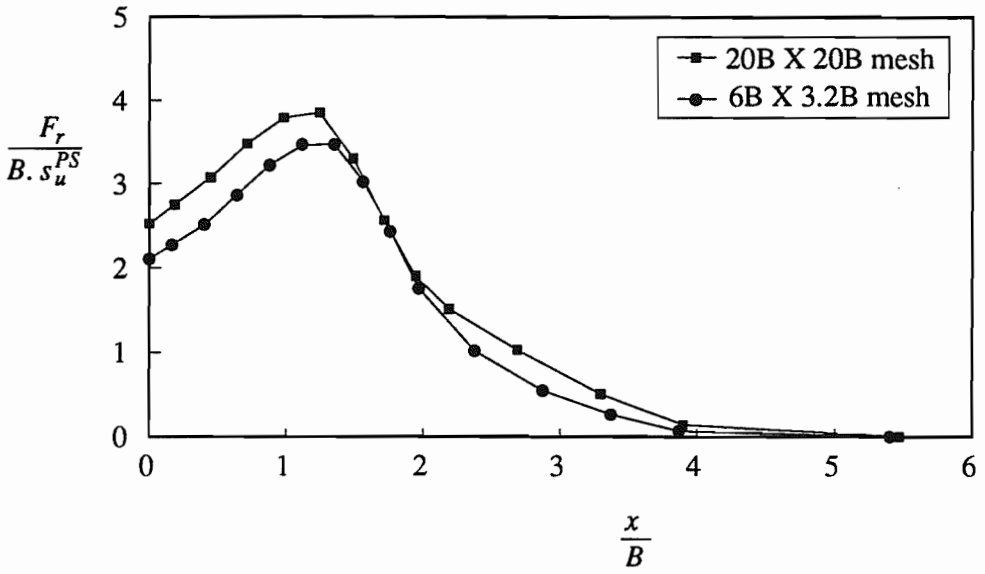

Figure 6.9: Reinforcement Tension ($F_r / (B\ s_u^{PS})$) for the Two Mesh Sizes, using the same Material Properties

6.3.4 Large and Small Displacement Analysis

Since the nature of an unpaved road allows large ruts to develop, it is argued that any numerical modelling of such structures should be based on large displacement, large strain theory so that all the deformations and mechanisms acting in the road are accurately modelled. However, there are numerous applications of reinforced aggregate layers overlaying soft ground for which any significant surface rutting is undesirable, as discussed in Chapter 1. In order to investigate any mechanisms of reinforcement that may act in a reinforced two-layer soil system, where the particular application requires that the displacements at the surface of the fill layer should be small, a small displacement, small strain finite element analysis should be used.

The objective of this section and the next is to study the mechanisms of reinforcement that operate in a reinforced two-layer soil system when there is no surface, or membrane deformation and then to investigate those additional mechanisms which may operate when large deformations are allowed to develop. To achieve this a comparison is undertaken of the plane strain finite element results obtained from the small and large strain analyses of

both a reinforced and an unreinforced two-layer soil system. These numerical results will also be compared to those predicted by the Houlsby *et al.* (1989) plane strain analytical design method, as discussed in the literature review Section 2.5.1.

The difference between small and large strain finite element analyses, is that in small strain the mesh geometry is not updated as the calculation proceeds, whereas geometric modifications are undertaken at each increment of displacement in large strain. In practical terms this means that for small strain the geometry of the finite elements remain unchanged during the loading process and that first order, infinitesimal, linear strain approximations can be used. By using a large strain analysis however, all of the geometric non-linearities associated with large displacements will be modelled accurately (as discussed in Section 3.2). The advantage of studying a small strain analysis is that the reinforcement mechanisms, that do not depend on geometric effects, become clearly visible. The 'tensioned membrane effect' for instance, is therefore explicitly excluded.

All of the research described in this section has been carried out using the finite element program OXFEM. Although this program is designed to conduct large displacement large strain calculations it has the facility to also carry out small displacement small strain analyses by simply by-passing the relevant large strain part of the program.

Four finite element runs are considered for this particular study of the different results obtained from large and small strain analyses of a reinforced and unreinforced two-layer soil system. The two-layer soil system dimensions and properties described in Appendix 6A are used with the large ($20B$ X $20B$) finite element mesh 'B', Figure 5.2. The system of referencing the plane strain finite element runs follows an order where the first letter gives the relevant mesh size (i.e. A, B or C, depending upon the particular fill depth D_f), the proceeding number refers to the fill friction angle in plane strain (i.e. $30°, 40°$ or $55°$) and the final letters indicate whether reinforcement is present ('R') or not, and whether it is a small strain ('S') or large strain analysis, e.g. B40R is a large strain reinforced finite element run using mesh B, with $\phi_{PS} = 40°$. The axisymmetric finite element runs are proceeded by 'AX'. For the corresponding Houlsby *et al.* (1989) and Houlsby and Jewell (1990) analytical

results the referencing is generally the same as for the finite element runs, but preceded by an 'R', e.g. RB40R. Some slight variations of this referencing scheme do occur in this dissertation, but these are self-evident.

A comparison of the footing load-displacement responses for each of the four finite element runs and the four corresponding analytical results is shown in Figure 6.10, where P is the average value of vertical stress beneath the footing and δ is the vertical footing displacement.

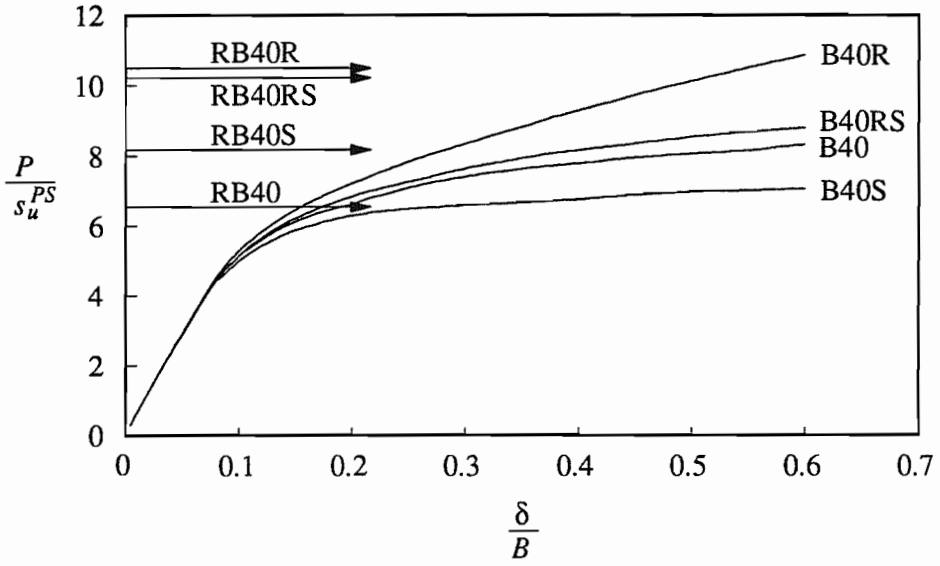

Figure 6.10: Pressure-Displacement Responses

By determining the value of a load spread angle, β, (as described in Section 6.3.5) and an angle of friction on the footing base, δ_f, (as described in Section 6.5.7) and using it in the Houlsby *et al.* (1989) method, along with the plane strain friction angle and clay strength, a direct comparison can be made of the results predicted by this analytical method and the calculated finite element results, i.e. the ultimate footing load (P_f) and the reinforcement tension (F_r).

Table 6.1 gives the run references and the final normalised footing pressures (P_f / s_u^{PS}) at a footing displacement of $\delta = 0.6B$ taken from Figure 6.10, as well as the calculated load

spread angles (β) and angles of footing base friction (δ_f). The values of δ_f are negative because the shear stresses at the footing-fill boundary are found to be outward acting. The 'R' denotes a reinforced analysis and 'U' an unreinforced analysis.

				F.E.		Analytical		
		δ_f	β	**Ref.**	P_f / s_u^{PS}	**Ref.**	P_f / s_u^{PS}	$F_r / (B\, s_s^{PS})$
Large Strain	R	−10.3°	40.9°	B40R	10.86	RB40R	10.49	3.28
	U	−8.0°	35.9°	B40	8.33	RB40	6.56	-
Small Strain	R	−3.0°	39.5°	B40RS	8.81	RB40RS	10.23	1.89
	U	−1.4°	37.6°	B40S	7.05	RB40S	8.16	-

Table 6.1: Run References for the Finite Element and Analytical Results shown in Figure 6.10

It is clear that the numerical load-displacement responses of the two large and two small strain finite element analyses are indistinguishable during the initial elastic loading, but that beyond a footing displacement of approximately $0.09\,B$ the curves begin to diverge significantly. This suggests that the presence of the reinforcement has no significant influence on the performance of the two-layer soil system within the elastic regime, but plays more of an important role once the system becomes subjected to plastic deformations, as found by Love (1984).

For the small strain runs, B40S and B40RS, the improvement in the load capacity of the structure by including reinforcement is about 25%, at the final footing displacement of $0.6\,B$, while for the equivalent large strain analyses the improvement between runs B40 and B40R is about 30%. This shows that the reinforcement has a greater effect in improving the bearing capacity of the two-layer soil system for a large displacement, large strain analysis than in a small strain one (as also shown by Burd and Brocklehurst (1991)).

The amount of strengthening due to the purely small displacement reinforcement mechanism of the 'shear stress effect', evident in Figures 6.14 and 6.15, can be measured directly from the difference between the small strain unreinforced and reinforced runs, i.e. a 25% better load capacity at $\delta = 0.6B$. The amount of additional improvement due to the large displacement reinforcement mechanisms, which develop as a result of the substantial rutting in the large strain analysis, can be estimated as the percentage difference between the final footing pressures for the small and large strain reinforced analyses, B40RS and B40R, i.e. approximately a 23% increase in bearing capacity. However, this 23% improvement can be attributed to both the influence of soil heave, which creates a surcharge and hence makes the entire system stiffer, as well as the reinforcement mechanisms of 'restraint' and 'tensioned membrane'.

The heave at the fill surface in a large displacement analysis creates an apparent improvement in the performance of the system. To calculate the true loading improvement obtained just through the purely large displacement reinforcement effects, the influence of any soil heave has to be removed. This can be quantified as the difference between the final footing loads for the small and large strain unreinforced analyses, B40S and B40, i.e. about 18%, therefore:-

Reinforced *large* strain improvement		Unreinforced *large* strain improvement		Tensioned membrane and restraint improvement
23 %	-	18 %	=	5 %

This effectively eliminates the surcharge effects at the surface for the large strain analyses.

This comparison illustrates well the need to use a large strain, large displacement formulation in the analysis of such two-layer soil systems if a complete finite element study of the reinforcement mechanism is to be conducted. Clearly, the geometric non-linear terms included in the finite element equations of a large strain analysis are necessary in order to capture all of the mechanisms of reinforcement. However, there is obviously a very important reinforcement mechanism acting in a two-layer soil system that does not rely on large

displacement effects, i.e. the 'shear stress mechanism'. There is also a comparatively minor 'improved load spread' of an extra 2° and 5° for these particular small and large strain analyses respectively, but this is not a general trend (as exhibited in Table 7.2).

Figure 6.10 also shows the ultimate footing loads predicted by the Houlsby *et al.* (1989) design method for the unreinforced systems (RB40 and RB40S) and the reinforced systems (RB40R and RB40RS). Although the analytical method is strictly a small displacement analysis its predictions can be compared with the results obtained from both the large and small displacement finite element solutions by using the appropriate values of β and δ_f, as given in Table 6.1.

Considering the small strain analyses first, it is evident that the Houlsby *et al.* (1989) method slightly overestimates the load capacity for both the reinforced and unreinforced systems, as predicted by the finite element analysis at a final footing displacement of $\delta = 0.6B$, (approximately 16% too high). Nevertheless the percentage of improvement between RB40S and RB40RS, approximately 25%, is equal to the final improvement between runs B40S and B40RS. For the large strain analyses, however, the analytical prediction of P_f for the reinforced system, RB40R, is a very good agreement to the finite element solution (approximately 3% too low), whereas the unreinforced prediction, RB40, is substantially lower than run B40 (21% less) because of the significant outward acting frictional force on the footing base ($\delta_f = -8.0°$). The analytical method assumes that this force increases the magnitude of the outward shear stresses on the clay surface, thus further reducing the bearing capacity of the clay, but in fact the shear stresses are found to be inward acting in the area directly below the footing (Figure 6.14). Therefore, the analytical estimate of the percentage improvement between the unreinforced and reinforced systems for a large displacement analysis is about 60%, as opposed to the 30% improvement in the numerical calculations. Clearly the Houlsby *et al.* (1989) method can be considered a reasonably accurate design tool for estimating the ultimate load bearing capacity of reinforced and unreinforced two-layer soil systems when surface deformations are insignificant, but it is less applicable to the case where large displacements can occur.

6.3.5 Stresses acting on Reinforcement and Interpretation of Load Spread

In order to investigate the mechanisms of reinforcement in greater detail it is instructive to inspect the normal and shear stresses acting at the soil-reinforcement interface for both a small and a large strain finite element analysis. These stresses are extracted from the interface elements used in the finite element solution in the simple manner discussed in Chapter 5.

First consider the normal stresses (σ) developed along the interface of the soils, measured from the footing centre-line (x), at a final footing displacement of $\delta = 0.6B$. Figure 6.11 shows the normal stresses acting at the unreinforced soil interface for the small and large strain finite element runs B40S and B40, and Figure 6.12 shows the corresponding small and large strain normal stresses that act when reinforcement is included, runs B40RS and B40R respectively.

Theoretical foundation design often assumes that imposed footing loads create a uniform pyramidal load distribution with depth through the soil and estimates are made of a constant load spread angle such as β, see Giroud and Noiray (1981), Sowers *et al.* (1982), Poran (1985) and Houlsby *et al.* (1989). In reality there is unlikely to be a definite line distinguishing the extent of the load spread, rather, a zone across which the imposed footing pressure diminishes to zero, as seen in Figures 6.11, 6.12 and Plates 6.3 and 6.4. The limits of this zone would be extremely difficult to measure accurately in any model test. However, they can be established directly from the finite element results by studying the normal stress profile along the reinforcement length and determining the horizontal co-ordinates between which the distribution curve sharply decreases, indicating the edge of the area affected by the imposed load.

To simplify the problem it is assumed within this dissertation that, allowing for the self weight of the fill, the edge of the imposed loaded area at the fill base is defined by that horizontal distance from the footing centre-line (B') which contains 95% of the imposed normal footing stress (σ^i) on the upper reinforcement surface. In this way, the 95% limit gives a theoretical load spread angle β. The process for determining this load spread angle is that the pressure due to the self weight of the fill is calculated and subtracted from the total normal stress at the fill base (σ) predicted by the finite element analysis. This will

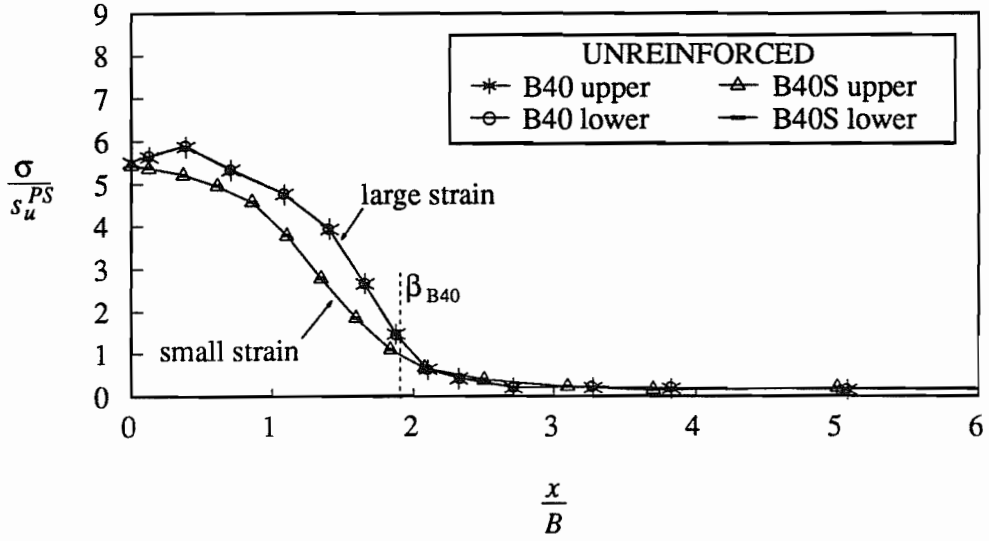

Figure 6.11: Normal Stresses acting at the Unreinforced Soil Interface (at $\delta = 0.6B$)

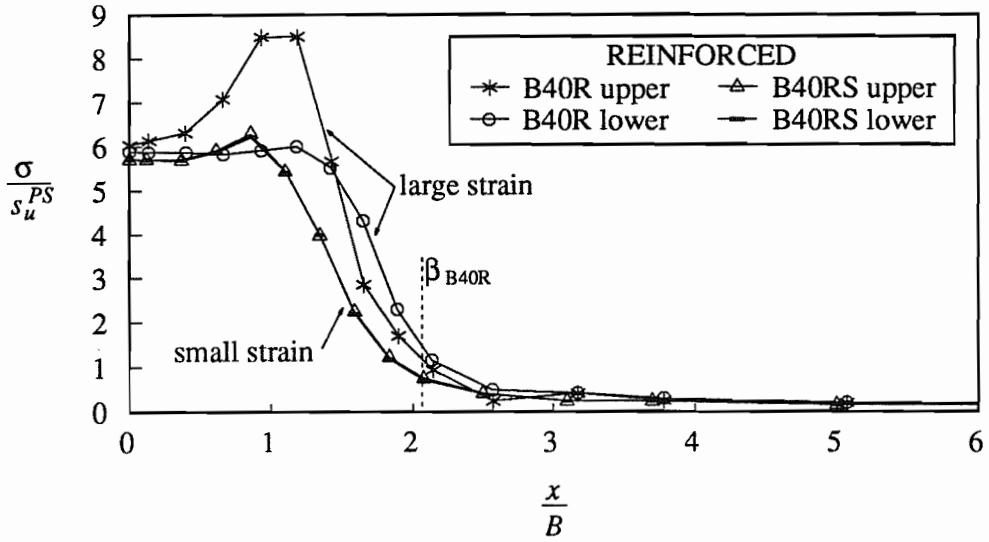

Figure 6.12: Normal Stresses acting on the Reinforcement Surfaces (at $\delta = 0.6B$)

then give the total imposed footing pressure along the reinforcement surface. A limiting point, from the footing centre-line, can be mathematically determined to give the exact cut-off for 95% of that full area under the normal stress curve influenced by the imposed footing load. This assumption means that a single value for the load spread angle can be obtained for any particular analysis.

Figure 6.11 actually shows four profiles of normal stress at the fill-clay interface, but the upper and lower stress distributions coincide for any particular run, because there is no reinforcement layer present. There is clearly a marked difference between the small strain and the large strain analyses within the region directly influenced by the footing load, the limit of which is shown by the load spread β_{B40}. The small and large strain, unreinforced, load spread angles (Table 6.1) would be almost at the same x co-ordinate, so only the large strain β value is plotted in Figure 6.11 and similarly for the reinforced case in Figure 6.12.

Considering the unreinforced analysis first the small strain normal stresses are at a maximum on the footing centre-line, where $\sigma = 5.43\, s_u^{PS}$, and they steadily decrease to the constant minimum surcharge, q, of $0.19\, s_u^{PS}$ which is due to the self weight of the fill ($q = \gamma_f D_f$). The large strain normal stresses start at $\sigma = 5.54\, s_u^{PS}$ on the centre-line and after increasing slightly to a maximum of $5.9\, s_u^{PS}$ they then decrease until merging with the small strain results just beyond the load spread limit, at approximately $x = 2.1\, B$.

It is established from the upper and lower bound plasticity theorems developed for simple indentation problems in metal (Calladine (1985)), that the 'exact' solution for the ultimate bearing capacity (P_u) of an elastic, perfectly plastic cohesive material which is being subjected to a purely vertical bearing capacity type failure, with an applied surcharge of q, is given by:-

$$P_u \;=\; N_c\, s_u^{PS} + q \;=\; (\pi + 2)\, s_u^{PS} + q \qquad (6.3)$$

where N_c is the bearing capacity factor and s_u is the undrained shear strength of the clay.

This plasticity theory predicts that the normal stresses transmitted onto the clay directly under the footing (Figure 6.11) should be at a constant value of $(\pi + 2)\, s_u^{PS} + q \;\approx\; 5.33\, s_u^{PS}$ within the load spread area, as shown schematically in Figure 6.13. Clearly the plane strain finite element computations of the normal stress do not give this theoretical constant distribution, which is because of the presence of some outward acting shear stresses (as discussed later), however the maximum normal stresses at the footing centre-line are calculated to be just 2% - 4% higher than the plasticity solution, as illustrated in Figure 6.13.

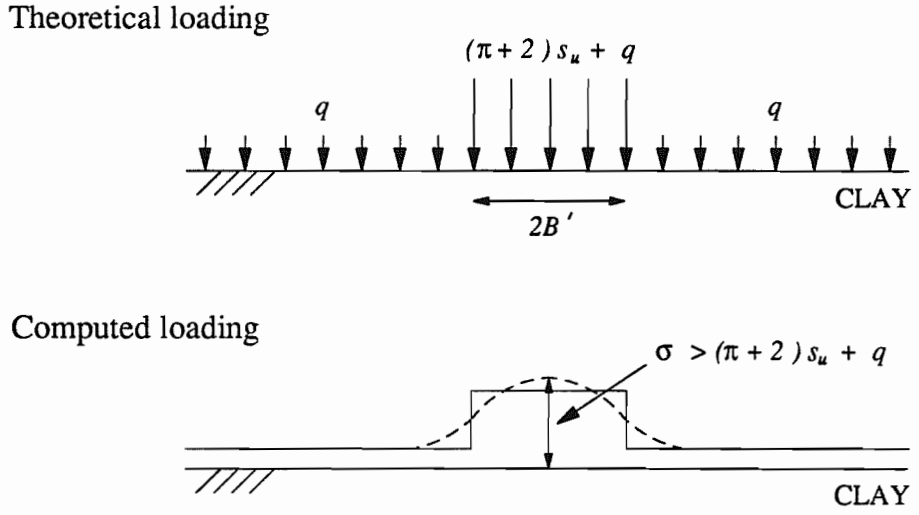

Figure 6.13: Simplified Distribution of Normal Stresses on Clay Surface

It is suggested that, because of the nature of the normal stress distribution, the additional loading at the edges of the load spread area ($2B'$) allows the peak normal stress at the footing centre-line to slightly exceed the ultimate bearing capacity (Houlsby (1992)).

The total normal force (i.e. the area under the normal stress curve) applied at the unreinforced interface in the large strain analysis is approximately 13% greater than that applied in the small strain analysis. This is mostly due to the extra amount of footing load needed to overcome the surcharge that is created by the fill heave at the footing edge, although the particular distribution of shear stresses along the clay surface also has some influence, which is discussed later.

Figure 6.12 shows similar distributions of normal stress along the soil interfaces for a small and large strain analysis, but for the case where reinforcement is included. Considering the small strain analysis first, the normal stresses along the upper and lower surfaces of the reinforcement coincide, because there are no geometric effects involved. The increase in the magnitude of the small strain force applied at the interface for the

reinforced case compared to the unreinforced case, is approximately 16%. Which is entirely due to the fact that greater footing loads need to be applied for the stiffer reinforced case in order to obtain the same footing displacement.

The small strain, reinforced, normal stress distribution is noticeably different to the unreinforced distribution in that σ equals the larger value of $5.71\, s_u^{PS}$ at the footing centre-line and remains relatively constant, increasing only slightly, between $x = 0 \rightarrow 0.9\, B$. The stress then decreases sharply to the permanent in-situ value of the fill self-weight at a point just beyond the calculated 95% load spread limit β_{B40R}.

Clearly, the horizontal extent of the area influenced by the footing pressure is slightly greater in the small strain reinforced case (B40RS) than for the small strain unreinforced case (B40S), i.e. $\beta_{B40RS} > \beta_{B40S}$. This would suggest that a small displacement reinforcement mechanism, of the form proposed by Giroud *et al.* (1984) involving an improvement of load distribution due to the inclusion of reinforcement, is operating in this two-layer soil system. Unfortunately the Giroud *et al.* (1984) design method only estimates the overall improvement due to the combined effects of subgrade confinement, load distribution and tensioned membrane (see Chapter 2), therefore no detailed predictions are given of how much improvement can be obtained in just the load spread angle. However, the increase in load spread for these particular small strain finite element calculations is only 5% for $s_u^{PS} = 30\, kPa$, unlike the 30% average improvement reported by Alenowicz and Dembicki (1990) for $s_u^{PS} = 7.4\, kPa$.

The profiles of the large strain reinforced normal stresses (run B40R) are prominently different for the upper and lower surfaces (Figure 6.12). They start at the footing centre-line almost identical at $6\, s_u^{PS}$ (which is about 12% greater than the ultimate vertical load capacity $P_u \approx 5.33\, s_u^{PS}$ given by equation (6.3), because of the inward acting shear stresses on the clay, Figures 6.15 and 6.16 Mode 2), but then differ in that the lower stress distribution remains constant up to $x = 1.2\, B$ and then drops sharply towards the load spread limit, which approximates to the plasticity theory solution of a constant load distribution. Whereas the upper large strain normal stress increases to a peak value of $8.5\, s_u^{PS}$ at the point where the curvature of the deformed membrane is greatest, before decreasing to the residual normal

stress. The normal force applied to the clay surface in the reinforced case (B40R) is 19% greater than that in the unreinforced (B40), but moreover the force on the upper surface applied by the fill base is 29% greater than in the unreinforced case. This larger amount of normal pressure sustained by the upper reinforcement surface compared to the lower surface is a consequence of the tensioned membrane action which develops at significant rut depths.

The 14% increase in the load spread for the large strain runs (between β_{B40} and β_{B40R}) is more substantial than the 5% achieved for the small strain runs (Table 6.1). However, these improvements are considered to be circumstantial since they are inconsistent with the changes in β for the parametric analyses listed in Tables 7.2, 8.1 and 10.1, where β is uninfluenced by the reinforcement.

Clearly a study of the normal stresses at the soil-reinforcement interfaces is instructive in investigating the mechanisms of reinforcement in greater detail, but likewise the shear stresses at the base of the fill and on the subgrade surface also have an important influence on the load bearing capacity of the two-layer soil system, i.e. the shear stress mechanism discussed in Chapter 2. Similar to Figures 6.11 and 6.12, the distribution of the small and large strain shear stresses (τ) across the reinforcement length (x), at a final footing displacement of $\delta = 0.6\,B$, are shown in Figures 6.14 and 6.15 for the unreinforced and reinforced cases, respectively. Shear stresses acting outwards from the footing centre-line are positive.

In the unreinforced analyses, Figure 6.14, the upper and lower shear stress profiles superimpose for each finite element run. For the small strain calculation (B40S) the shear stresses are negligible directly under the footing, but reach a maximum that is equivalent to the clay shear strength ($1\,s_u^{PS}$) at about $x = 1.6\,B$. This peak of outward shear signifies some sliding between the clay and fill, localised at this point. The large strain calculation (B40) has more significant inward acting shear stresses in the area directly under the footing ($\tau = -0.8\,s_u^{PS}$), but these change direction beyond $x = 1.2\,B$ and, as with the small strain analysis, an outward maximum of $1\,s_u^{PS}$ is reached at $x = 1.9\,B$, which is the exact point of the load spread limit β_{B40}.

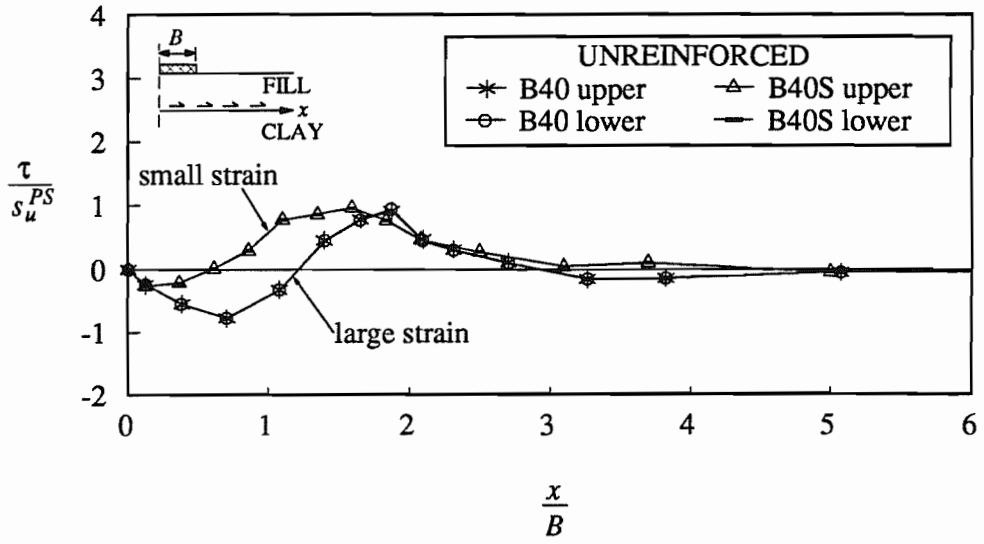

Figure 6.14: Shear Stresses acting at the Unreinforced Soil Interface (at $\delta = 0.6B$)

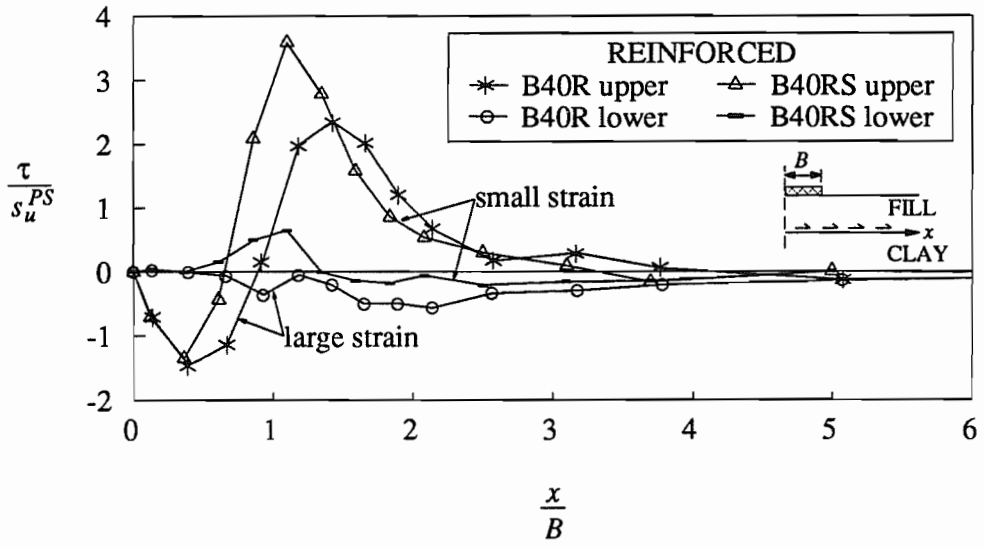

Figure 6.15: Shear Stresses acting on the Reinforcement Surfaces (at $\delta = 0.6B$)

Outward acting shear stresses have the detrimental effect of reducing the bearing capacity of the subgrade (shown by Bolton (1979) and illustrated in Figure 6.16 as Modes 3 and 4), so that failure will occur at less than the ultimate vertical load capacity of $P_u = (\pi + 2)\, s_u^{PS} + q$. The presence of these outward shear stresses, therefore, has the effect of progressively decreasing the magnitude of the normal stresses away from the footing centre-line, as is apparent in Figure 6.11. However, inward acting shear stresses directly under the footing, as are present for the large strain analysis, will moderately enhance the

clay strength locally, which is also partly why the large strain normal stresses are slightly greater than the small strain ones in Figure 6.11 (although the soil heave at the fill surface is thought to have the greater influence).

In the reinforced analyses, Figure 6.15, the footing load has to be larger to attain the same footing displacement and consequently the shear stresses are also higher. Note that the shear stresses on the upper reinforcement surface are significantly larger than those in the unreinforced case. Inward shears of around $-1.5\, s_u^{PS}$ develop directly under the footing and outward shears reach a peak of $\tau = 3.6\, s_u^{PS}$ for small strain (B40RS) and $\tau = 2.4\, s_u^{PS}$ for large strain (B40R). The small strain lower shear stresses vary between zero initially, to outward acting (with a maximum of $0.7\, s_u^{PS}$) and then to low inward acting, while the large strain lower shear stresses remain inward acting throughout (maximum of $\tau = -0.6\, s_u^{PS}$). It is this consistent inward shear stress (Mode 2 in Figure 6.16), which generates the higher load bearing capacity of approximately $1.11 \times 5.33\, s_u^{PS} \approx 6\, s_u^{PS}$ seen in the large strain normal stress plot, Figure 6.12.

The small and large strain shear stresses on the underside of the reinforcement are relatively minor in comparison to both those shears acting on the upper reinforcement surface and those acting on the clay surface for the unreinforced case. This clearly illustrates the shear stress mechanism, where the reinforcement actually reduces the amount of outward clay shear stress and therefore increases its load bearing capacity. Furthermore, the reinforcement has the beneficial effect of increasing the amount of inward acting shear stress, especially for the large strain analysis, which will significantly enhance the strength of the clay. Using the theory of slip-line fields (Calladine (1985)) it is found that an 11% improvement in the ultimate bearing capacity of the clay can be obtained if the inward acting shear stresses, outside of the load spread area, reach the value of the clay shear strength, i.e. if $\tau = s_u^{PS}$ for Mode 2 in Figure 6.16.

These finite element investigations of the interface stresses reveal the reinforcement mechanisms operating in a two-layer soil system extremely effectively. It is apparent from these investigations, however, that the actual distribution and arrangement of the normal

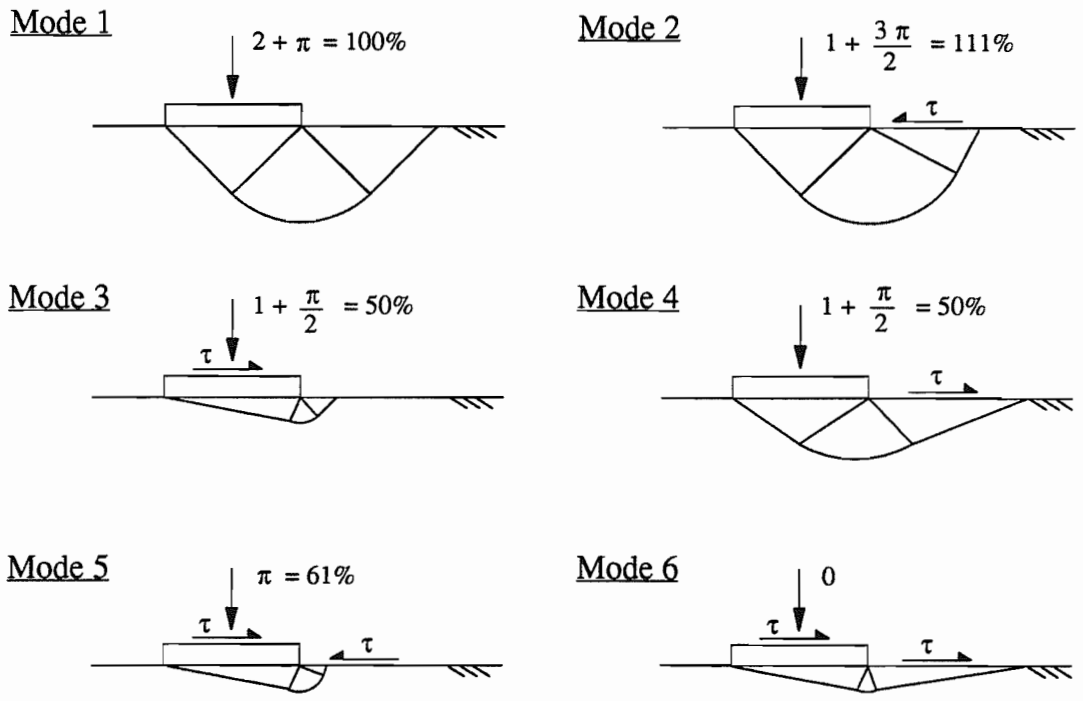

For $\tau = s_u$

Figure 6.16: Exact Plane Strain Bearing Capacity Factors (N_c) for various Clay Failure Mechanisms (Shown schematically)

and shear stresses in the unreinforced and reinforced situation, for small and large strain analyses, is much more complex than the simplistic assumptions made in the Houlsby *et al.* (1989) design method.

The distributions of the large and small strain reinforcement forces (F_r) are extracted from the finite element calculations by averaging the three Gauss point forces, per plane strain membrane element, and then plotting that average elemental force at the mean x co-ordinate of the Gauss points, as shown in Figure 6.17.

The tension induced in the reinforcement is due to the horizontal forces applied to it by the fill layer above and the clay subgrade below (as described in Burd and Brocklehurst (1990) and Kwok (1987)). Clearly there is a larger force developed throughout the reinforcement for a large strain analysis (B40R) compared to that for a small strain analysis

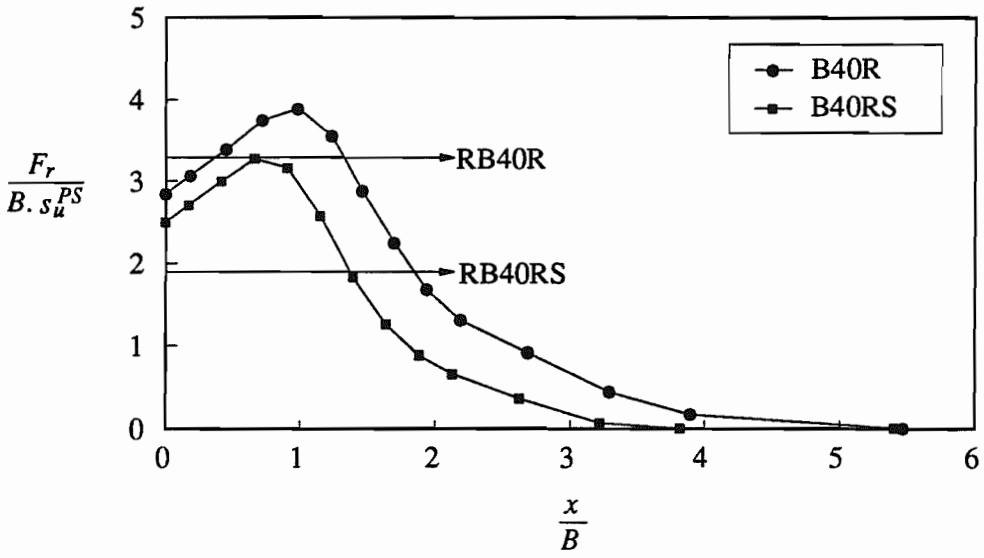

Figure 6.17: Reinforcement Tension (at $\delta = 0.6B$)

(B40RS). At the centre-line the large strain reinforcement tension is 14% greater than for the small strain and the large strain peak tension is 19% greater than the small strain peak. Large displacement analyses evidently generate higher reinforcement forces due to the imposed deformation and the increased amount of force applied.

The Houlsby *et al.* (1989) analytical predictions of the small (RB40RS) and large (RB40R) displacement reinforcement tensions are shown in Figure 6.17. The reason the limit equilibrium design method underestimates the peak reinforcement forces is because of the inaccurate arrangement of stresses assumed in the analytical method. For instance, there is no consideration of the shear force applied to the reinforcement by the clay subgrade, which is in fact comparatively significant as illustrated in Figure 6.15. Furthermore, the analytically predicted value of F_r is sensitive to the magnitude of the footing friction force ($P_f B \tan\delta_f$), which for RB40RS is lower than for RB40R, because of the smaller angle of friction at the footing base (Table 6.1).

6.3.6 Conclusions from Preliminary Experiments

The preliminary plane strain finite element studies, discussed in this Section 6.3, produced several important conclusions relevant to the selection of the most appropriate numerical

approach for the parametric study, for example;

Refinement of a finite element mesh (i.e. increasing the number of elements and therefore nodes) leads to a greater accuracy in the numerical calculation, but at the expense of computing time. A balance has to be found so that the analysis is relatively efficient and practical, but with an acceptably small inherent error. The typical plane strain mesh that was finally chosen for the parametric study, after the completion of a convergence study (Section 6.3.2), is shown in Figure 5.2. The ratio of the width of the mesh to the element side length, of the smallest element employed in the mesh, is 350 and for the largest element is 3.

Using too small a mesh spuriously increases the elastic stiffness of the load-displacement response, but then decreases the plastic stiffness, so that the predicted final load bearing capacity of the system is considerably reduced (by $\approx 20\%$). The interface stresses and reinforcement forces are also influenced by the position of the mesh boundaries, particularly the normal stresses which are significantly reduced if the boundaries are too close to the footing. The minimum mesh width capable of negating the boundary effects is believed to be about $10\,B$ and the minimum overall depth is approximately $13.2\,B$ (including $1.2\,B$ depth of fill).

A large displacement, large strain type analysis is essential in order to capture fully all the reinforcement mechanisms acting in a two-layer soil system. However, the shear stress mechanism of the reinforcement, which reduces both the shear stress magnitude and the area of the clay surface it influences, operates even if there is no surface rutting or membrane deformation. This small displacement mechanism, combined with a slightly increased load spread, provides the greatest amount of improvement in the load bearing capacity, accounting for about 25% strengthening in the particular case considered. In a large strain analysis, where significant membrane deformations can occur, these small displacement mechanisms have an increased influence and the additional large displacement tensioned membrane and restraint mechanisms also develop. These geometrically non-linear effects occur as a result of substantial rutting and contribute an extra 5% to the overall loading improvement obtained for this specific case.

Therefore, the design methods for two-layer soil systems, such as unpaved roads, need to take account of both the small displacement reinforcement mechanisms and those mechanisms which, it has been shown, also act at large displacements. The Houlsby *et al.* (1989) method is shown to provide good approximations to both the small displacement unreinforced and reinforced limit loads. It is also capable of accurate predictions to the large displacement reinforced load, although less exact in predicting the large displacement unreinforced load and the reinforcement forces.

A method is proposed of estimating the load spread angle, β, from the upper interface normal stress distributions. This provides a consistent parameter which can be compared in each of the finite element studies to assess the influence of a particular variable.

6.4 Comparison of Plane Strain and Axisymmetric Analyses

A comparison of a plane strain and an axisymmetric large strain analysis is done for the 'central parametric analysis' using the material properties and dimensions defined in Appendix 6A, for the unreinforced and reinforced cases.

The plane strain finite element mesh with six-noded continuum elements, three-noded reinforcement elements and six-noded interface elements is shown in Figure 5.2 and the corresponding axisymmetric mesh with fifteen-noded continuum elements, the new five-noded reinforcement elements and ten-noded interface elements is shown in Figure 6.18. To obtain an accurate comparison between the finite element results the overall dimensions of the two meshes are identical and a similar number of nodes are used in each analysis. The plane strain mesh contains 1036 nodes and the axisymmetric mesh contains 1197 nodes. The footing radius, R, for the axisymmetric analysis is equal to the footing half width, B, for the plane strain analysis, i.e. $R = B = 0.25\,m$.

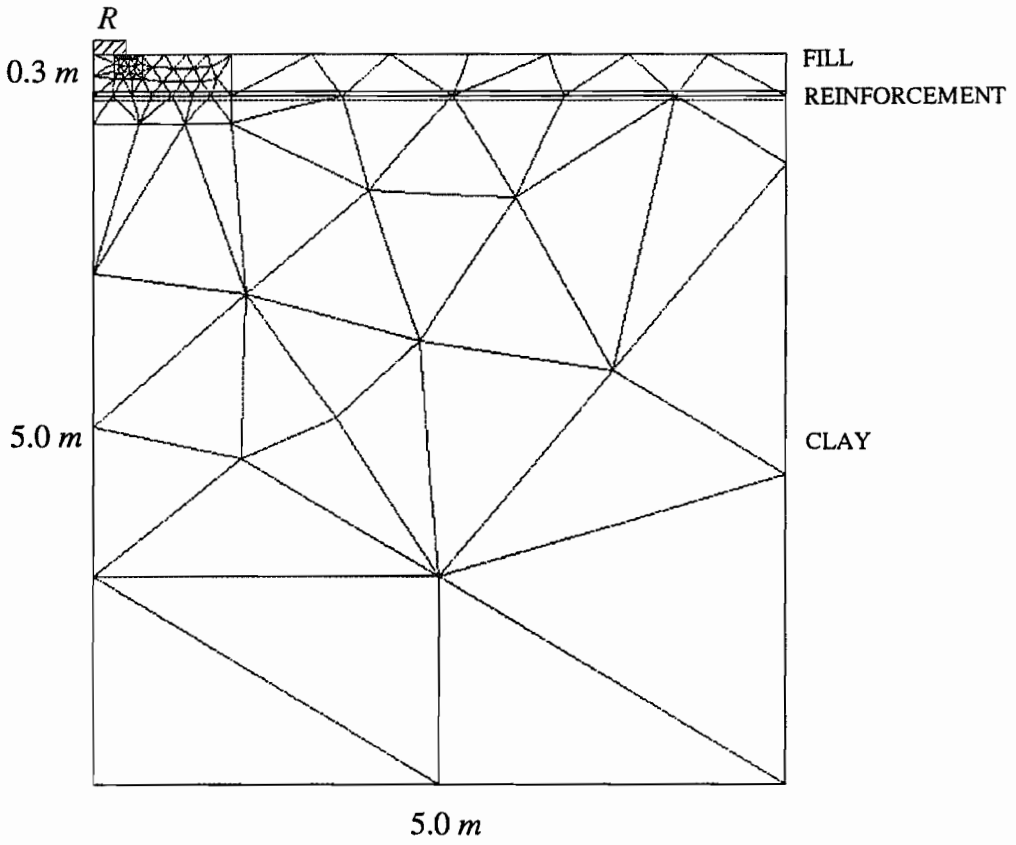

Figure 6.18: Axisymmetric Finite Element Mesh AXB

6.4.1 Load-Displacement Response

The footing pressure-displacement responses for each of the four large strain finite element runs are illustrated in Figure 6.19 and the results are presented in Table 6.2, where P is the average value of vertical stress beneath the footing and δ is the vertical footing displacement.

Using the load spread angles, β (as determined by the 95% load spread limit method), and the angles of friction of the footing base, δ_f (calculated by the procedure described in Section 6.5.7), each given in Table 6.2, a direct comparison can be made between the calculated finite element results and the results predicted by the analytical methods proposed by Houlsby *et al.* (1989) for plane strain conditions and Houlsby and Jewell (1990) for axisymmetric conditions (see Chapter 2). The ultimate footing pressures, P_f, given by the two analytical methods are shown in Figure 6.19 and tabulated in Table 6.2, where the 'R' denotes a reinforced analysis and 'U' an unreinforced analysis.

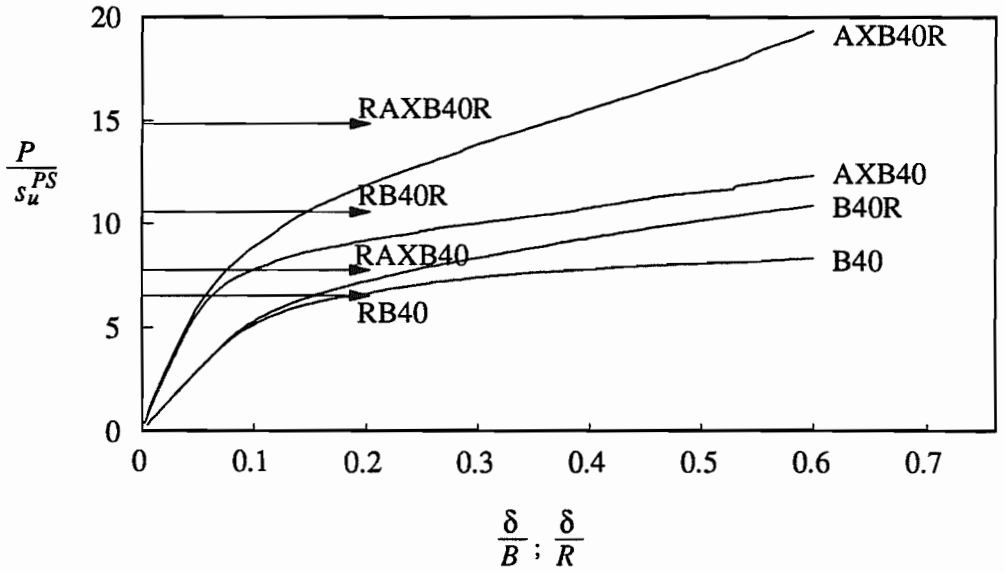

Figure 6.19: Pressure-Displacement Responses for Plane Strain and Axisymmetric Analyses

				F.E.		Analytical		
		δ_f	β	Ref.	P_f / s_u^{PS}	Ref.	P_f / s_u^{PS}	$F_r / (B\, s_s^{PS})$
Axi	R	−6.5°	27.2°	AXB40R	19.35	RAXB40R	14.87	2.53
	U	−10.5°	29.8°	AXB40	12.31	RAXB40	7.78	-
P.S.	R	−10.3°	40.9°	B40R	10.86	RB40R	10.49	3.28
	U	−8.0°	35.9°	B40	8.33	RB40	6.56	-

Table 6.2: Run References for the Finite Element and Analytical Results Shown in Figure 6.19

The initial finite element pressure-displacement responses for the axisymmetric analyses are a little more than twice as stiff as the responses for the plane strain analyses. Furthermore the responses for the axisymmetric unreinforced and reinforced analyses diverge at about $\delta = 0.05\,R$, whereas the corresponding plane strain analyses do not separate until about $\delta = 0.09\,B$.

At the final vertical footing displacement of $\delta = 0.6\,R;B$ the improvement in the load capacity of the system by including reinforcement in the axisymmetric analysis is about 57%, while the improvement for the plane strain analysis is only 30%. Additionally, the stiffer response of the reinforced axisymmetric analysis beyond $\delta = 0.2\,R;B$, compared to the reinforced plane strain analysis, is due to the increased amount of tensioned membrane effect. This shows that the reinforcement has a greater effect in improving the allowable loading on the two-layer soil system under axisymmetric conditions compared to plane strain conditions.

The ultimate footing loads predicted by the Houlsby *et al.* (1989) and Houlsby and Jewell (1990) analytical methods, Table 6.2, tend to underestimate the finite element results, particularly in the axisymmetric case. This is because of the limitation of the analytical methods to small footing displacements, whereas large displacements are allowed to develop in the large strain finite element solutions. Moreover, these methods are applicable to unpaved road design and if an unpaved road becomes rutted, then it is clear that the geometry of the system is such that the loading cannot be treated as axisymmetric.

The analytically predicted improvements in P_f from including reinforcement are overestimated, especially in the axisymmetric case where the improvement is estimated at approximately 91%, compared to the 57% improvement in the finite element solutions. This is because the unreinforced limit loads are predicted too low, due to the erroneous assumption that there are constant outward acting shear stresses at the unreinforced clay surface and that these are increased by the outward frictional forces on the footing base, therefore further decreasing N_c , whereas the shear stresses directly under the footing are actually found to be inward acting, Figure 6.20.

No significant changes occur in the load spread angles, given in Table 6.2, between the reinforced and unreinforced analyses, but there is a general decrease in β between the plane strain and axisymmetric cases. This is because the axisymmetric load spread gives a more rapid reduction of vertical stress within the fill than occurs in plane strain, as concluded by Milligan *et al.* (1989).

6.4.2 Normal and Shear Stress Distributions

The normal (σ) and shear (τ) stress distributions along the upper and lower reinforcement surfaces, at the final footing displacement of $\delta = 0.6\,B;\,R$, are extracted from the appropriate interface elements and shown in Figure 6.20 normalised with respect to the plane strain value of s_u^{PS}. For all the plane strain analyses the three Gauss point stresses for each interface element are averaged and plotted at the mean horizontal distance from the footing centre-line in order to obviate spurious oscillations, whereas for the axisymmetric analyses the seven Gauss point stresses for each interface element are plotted individually.

The differences between the axisymmetric and plane strain stress distributions plotted in Figure 6.20 are, on the whole, small. For the unreinforced case the axisymmetric normal stresses, which are slightly greater than the plane strain normal stresses directly under the footing, start at $\sigma = 5.48\ s_u^{PS}$ on the centre-line and increase to a maximum of $\sigma = 7.05\ s_u^{PS}$ within a small horizontal distance, beyond which the stresses decrease steadily to the constant surcharge of the fill self weight ($q = \gamma_f D_f$).

In Section 6.3.5 the magnitude of the plane strain normal stresses on the clay surface was compared to the ultimate bearing capacity (P_u) predicted by plasticity theory, equation (6.3). For the case of purely vertical loading in plane strain conditions the bearing capacity factor, N_c, is exactly equal to $(\pi + 2)$ and if outward shear stresses act on the clay surface the reduction in N_c can be expressed analytically. However, for the axisymmetric case the calculation of N_c cannot be done analytically, but it may be estimated by the method of characteristics. Houlsby and Jewell (1990) give a table of combinations of N_c and the average outward shear stress calculated using the "Fields" program developed by Professor G. T. Houlsby at the University of Oxford. The full bearing capacity, for purely vertical loading, is found to be 5.69.

Unlike the plane strain case the axisymmetric normal stresses illustrated in Figure 6.20 cannot be related to the plasticity calculations of P_u using $N_c = 5.69$, because this represents the collapse load for a Tresca material and the clay is represented in the finite element solution as an elastic-perfectly plastic von Mises material (Chapter 3), for which there is no known exact collapse load. However Yu (1990) shows that the von Mises collapse load is

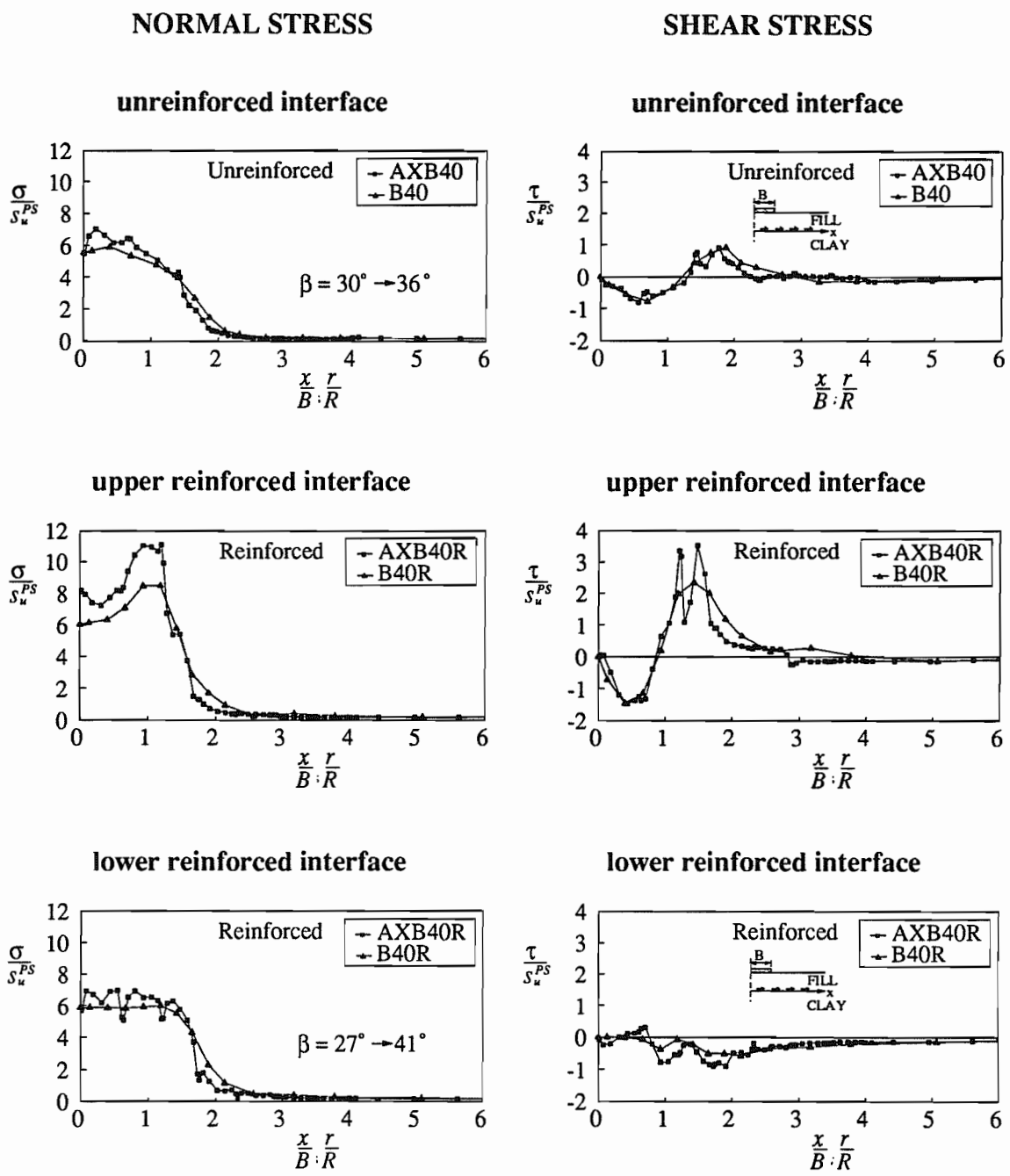

Figure 6.20: Normal Stress (σ / s_u^{PS}) and Shear Stress (τ / s_u^{PS}) along Interface for Plane Strain and Axisymmetric Analyses, (at $\delta = 0.6\,B; R$)

greater than the solution for a Tresca material and less than the solution for the Tresca material multiplied by a factor of $2/\sqrt{3}$. This is because in triaxial stress states the von Mises yield surface is equivalent to the Tresca yield surface and in plane strain conditions the von Mises yield surface represents the Tresca surface scaled by a factor of $2/\sqrt{3}$. The

stress state created by the circular load spread area at the fill base (synonymous to a loaded circular smooth footing) corresponds neither to a triaxial stress state nor plane strain conditions. The actual collapse load for a circular smooth footing resting on a von Mises soil is shown by Yu (1990) to be approximately $N_c \approx 6.3$. Therefore the normal stress on the clay surface within the load spread area for the axisymmetric finite element runs, when no shear stresses act, can be expected to be a constant value of:-

$$P_u = N_c s_u^T + q \approx 6.3 \frac{\sqrt{3}}{2} s_u^{PS} + q \tag{6.4}$$

Clearly the axisymmetric normal stresses at the unreinforced fill-clay boundary do not give this theoretical uniform distribution of $\sigma = 5.46\, s_u^{PS} + q = 5.46\, s_u^{PS} + 0.19\, s_u^{PS} = 5.65\, s_u^{PS}$ for the particular value of $\gamma_f D_f$, which is because of the outward acting shear stresses beyond $r = 1.2\, R$ shown in Figure 6.20. However, the normal stress at the footing centre-line is only 3% smaller than the plasticity solution, which is a good agreement. Similarly, the plane strain normal stress at the footing centre-line is just 4% greater than the plasticity solution given by equation (6.3), as discussed in Section 6.3.5.

The unreinforced axisymmetric and plane strain shear stresses initially act inwards, reaching a maximum of about $\tau = -0.8\, s_u^{PS}$, and then reverse direction to become significant outward shear stresses of $\tau = 1\, s_u^{PS}$, which cause the reduction in the normal stresses. Beyond about $r = 3\, R$ and $x = 3\, B$ the shear stresses remain as very small inward acting stresses.

The reinforced upper normal stresses are rather larger for the axisymmetric case than for the plane strain case, within the area directly under the footing, illustrating the greater tensioned membrane effect, see Section 6.4.1. However the reinforced lower normal stresses for the axisymmetric and plane strain cases are less disparate. The lower normal stresses for the axisymmetric case show a few spurious oscillations, the slightly smaller plane strain normal stresses showed some similar oscillations before a procedure of averaging Gauss point stresses was used. The expected constant value of σ within the load spread area, given by plasticity theory, is $\approx 5.65\, s_u^{PS}$ for axisymmetry and $\approx 5.33\, s_u^{PS}$ for plane strain. In comparison the axisymmetric finite element solution gives $\sigma_{axi} = 5.68\, s_u^{PS}$ at the footing centre-line (which is 0.5% larger than the theoretical prediction) and an average of $6.26\, s_u^{PS}$

between $r = 0 \rightarrow 1.2\,R$, which is 11% larger than the plasticity answer, while the plane strain finite element solution gives a consistent $\sigma_{PS} = 6\,s_u^{PS}$ between $x = 0 \rightarrow 1.2\,B$, which is approximately 12% larger. These increased normal stresses are due to the inward acting shear stresses on the clay outside of the load spread area (Figures 6.20 and 6.16 Mode 2). For the limiting case where $\tau = -1\ s_u^{PS}$ the exact increase in N_c can be estimated analytically in the plane strain case, as given in Figure 6.16, whereas in axisymmetry this is not possible, although it is likely that the increase is of approximately the same magnitude.

The reinforced axisymmetric and plane strain upper shear stresses are very alike and follow a similar distribution pattern to that of the unreinforced shear stresses, but reach much higher magnitudes because of the larger P_f needed to attain the same δ. The outward acting axisymmetric upper shear stresses display a more erratic distribution with a spuriously fluctuating peak value, compared to the plane strain, but the overall trends are very similar.

The reinforced axisymmetric and plane strain lower shear stresses are again quite comparable. Between $r = 0 \rightarrow 0.8\,R$ and $x = 0 \rightarrow 0.8\,B$ the shear stresses are zero for the plane strain case and vary from very small inward to very small outward for the axisymmetric case, respectively. Beyond this point the shear stresses maintain a continually inward acting distribution, with a peak of $-1\ s_u^{PS}$ for the axisymmetric analysis and $-0.6\ s_u^{PS}$ for the plane strain analysis.

6.4.3 Reinforcement Tension Distribution

The longitudinal reinforcement tension, F_r, in the plane strain analysis and the tangential and circumferential tensions in the axisymmetric analysis, at the final footing displacement of $\delta = 0.6\,R;B$ are plotted in Figure 6.21. The value of F_r in the plane strain case is calculated as the average of the three Gauss point forces per plane strain membrane element, whereas each axisymmetric membrane element Gauss point is plotted individually.

The axisymmetric tangential and circumferential membrane tensions show a similar pattern of distribution, but with the tangential reaching a peak of about $F_r = 4\ s_u^{PS}$ and the circumferential a peak of only $F_r = 3.4\ s_u^{PS}$. Beyond $r = 2.2\,R$ the tangential membrane tension reduces to zero quickly, in terms of horizontal distance, while the circumferential

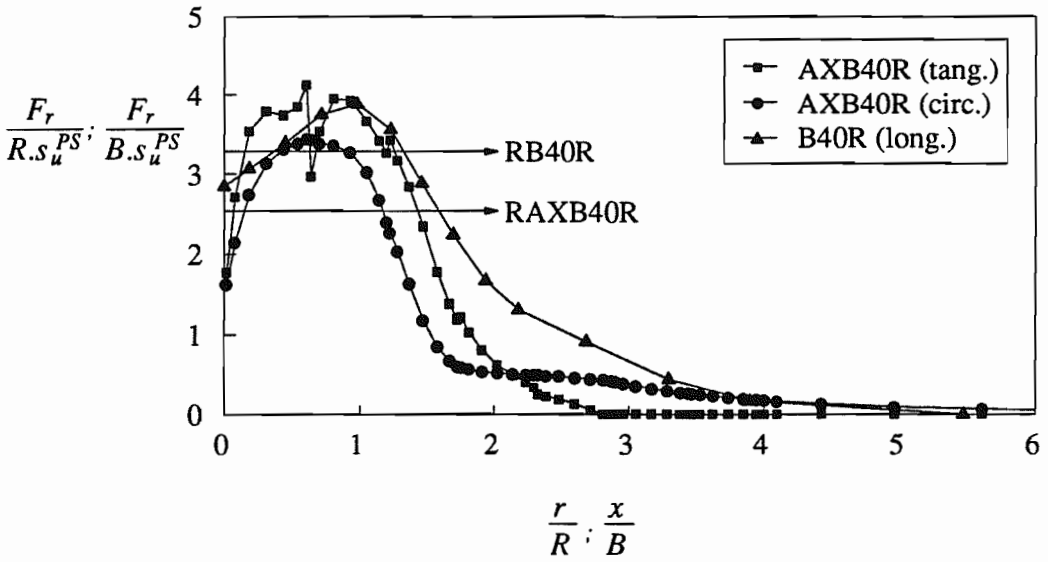

Figure 6.21: Reinforcement Tension for Plane Strain and Axisymmetric Analyses, (at $\delta = 0.6\,B; R$)

tension decreases to zero over a much larger distance. By comparison the plane strain longitudinal membrane tension reaches a maximum approximately equal to the peak axisymmetric tangential tension, but decreases more gradually than either of the axisymmetric tensions. This is because the load spread area in the plane strain analysis is larger than in the axisymmetric analysis and consequently the horizontal forces applied to the membrane by the upper and lower shear stresses extends over a greater horizontal distance.

Both the Houlsby *et al.* (1989) prediction of the reinforcement force for the plane strain case (RB40R) and the Houlsby and Jewell (1990) prediction for the axisymmetric case (RAXB40R) underestimate the peak reinforcement forces from the equivalent finite element solutions, as shown in Figure 6.21. This is because of the inexact simplified stress distribution assumed in these analytical methods.

6.5 Results of the Plane Strain and Axisymmetric Central Analyses

The final results from the unreinforced and reinforced plane strain and axisymmetric central parametric analyses (B40, B40R, AXB40 and AXB40R as defined in Appendix 6A) are presented fully in this section and a detailed investigation of the finite element runs is

undertaken. The 'plates', referred to in the proceeding sections and presented in Appendix 6B, were obtained from the two-dimensional contouring program '2Can' written by Professor G. T. Houlsby at the University of Oxford.

The areas of investigation are; 1) the deformations within the meshes directly under the footing at the end of the analyses, 2) the actual nodal displacements within the area of greatest deformity, 3) the horizontal strains under the footing, 4) the normal and shear stress distributions under the footing, 5) the principal stress directions in the fill, 6) the mobilised angle of friction for the fill, and 7) the stress distributions on the underside of the footing and the corresponding angle of friction of the footing base.

6.5.1 Deformed Meshes and Interface slip

The final deformed plane strain and axisymmetric meshes, within the footing area, for the unreinforced and reinforced analyses are shown in Figures 6.22 a) and b).

Clearly there is a reduced amount of deformation and heave in the fill layer for the reinforced analyses, compared to the unreinforced ones. Note the one single overturned continuum element at the fill surface, just at the outside edge of the footing in both the plane strain and axisymmetric deformed meshes, which has occurred because of excessive displacement. This does not significantly effect the accuracy of the results, but could be avoided by using an even higher density of elements within this area of large deformation.

The lines of displaced interface and/or membrane elements are illustrated in Figure 6.22 by a slightly thicker line. Directly under the footing there is no visible evidence of slip between the upper and lower surfaces of the boundary in the unreinforced or the reinforced analyses, but at the point of reverse curvature there is a small amount of observable slip in both analyses. This is reflected in Figure 6.23, which shows the relative movement (u_r) at the unreinforced and reinforced soil interfaces for the plane strain and axisymmetric analyses. Positive u_r indicates movement of the upper surface to the right relative to the lower surface. In axisymmetry slipping occurs within $r = 4\,R$ of the footing centre-line, whereas for plane strain slip continues to occur up to $x = 6\,B$. The slip at the unreinforced and upper reinforced interfaces is initially negative with the clay moving out from under the fill, generating the

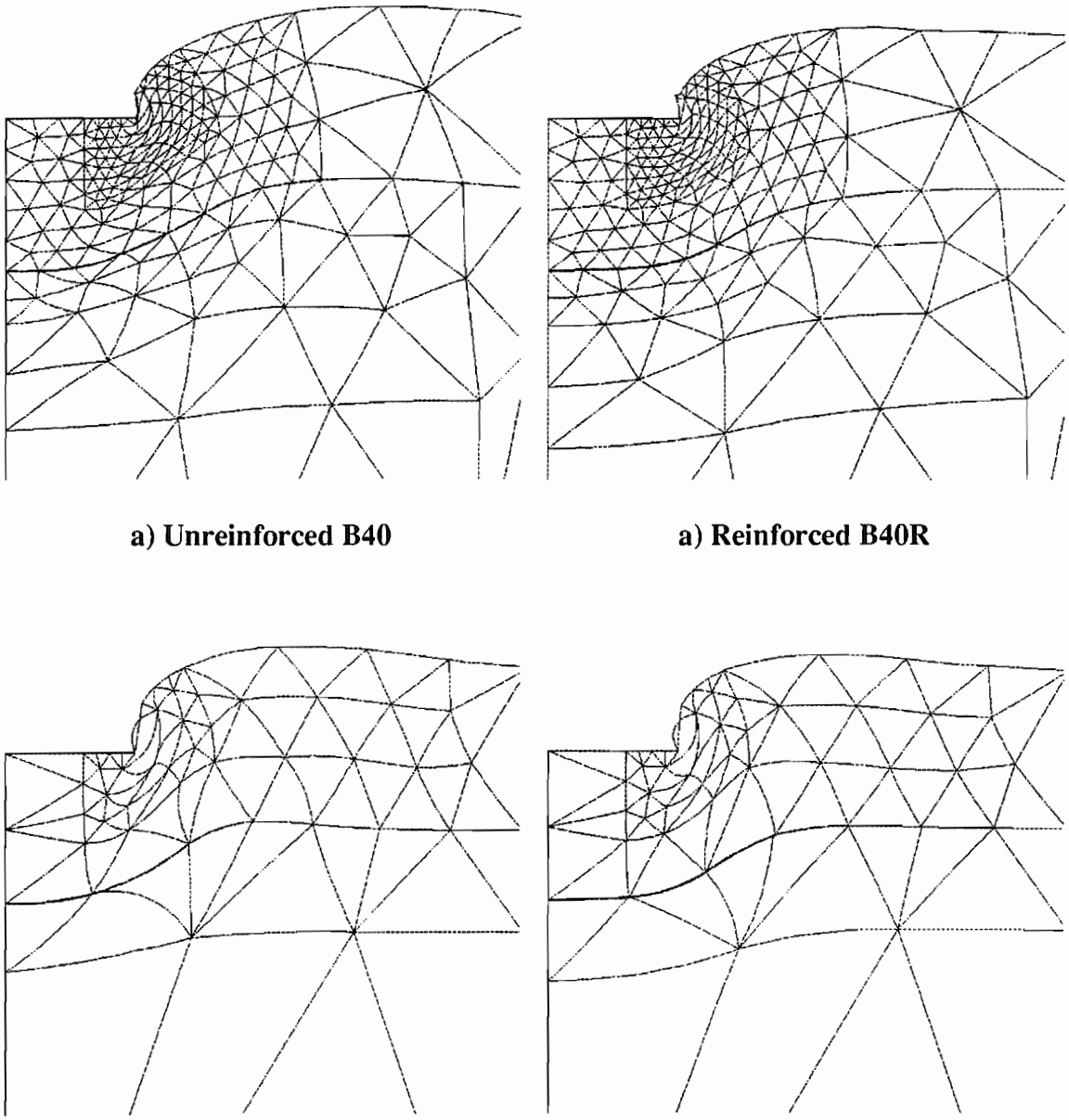

a) Unreinforced B40 **a) Reinforced B40R**

b) Unreinforced AXB40 **b) Reinforced AXB40R**

Figure 6.22: Deformed Meshes; a) Plane Strain, b) Axisymmetry

inward shear stresses shown in Figure 6.20, but then reverses at $x; r \approx 1.5\,B; R$, which develops the outward shear. The lower reinforced interface sustains consistently negative slip and therefore inward shear, i.e. the shear stress mechanism of the reinforcement. Beyond about $3\,B; R$ the slip does not generate any significant shear because of the small amount of normal stress acting.

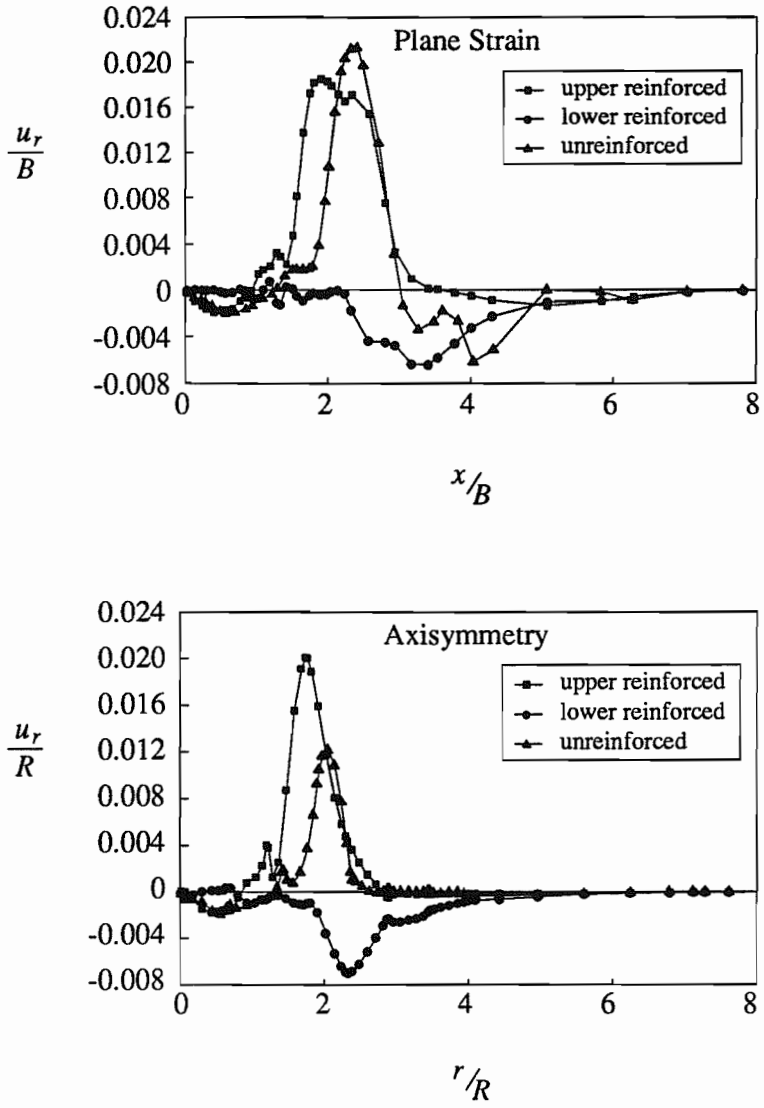

a) Plane Strain and b) Axisymmetry

Figure 6.23: Relative Slip (u_r) along Interfaces

6.5.2 Nodal Displacements

The nodal displacement vectors within the area of high deformation are illustrated without magnification in Figures 6.24 a) and b), Appendix 6B, for the plane strain and axisymmetric analyses. The initial positions of the footing and the boundary between the fill and clay are shown.

On comparing the unreinforced and reinforced nodal displacement vector plots in Figure 6.24 it is clear that when reinforcement is included both the magnitude of the displacements is greatly reduced and the mechanism of deformation alters for both plane strain and axisymmetry. For the unreinforced analyses the mode of deformation appears to be similar to that illustrated in both Figure 6.2 and Figure 6.16 Mode 1, where the change in the material type has little effect. Incorporating the reinforcement, however, has the effect of developing separate deformation mechanisms in each material, where the fill has a confined deformation zone just outside of the load spread, while the failure within the clay extends deeper as illustrated by the areas of yield in Figures 6.5 and 6.26. Immediately beneath the footing, for the unreinforced and reinforced cases, the fill is subjected to a rigid wedge type displacement. Although in plane strain and axisymmetry the changes in the deformation characteristics between unreinforced and reinforced are similar, the magnitude of the displacements reduces more quickly, in terms of distance, for axisymmetry.

6.5.3 Horizontal Strains in the Fill

The horizontal strains in the fill and clay layers for the plane strain and axisymmetric analyses are shown in Plates 6.1 and 6.2 Appendix 6B, respectively, for the unreinforced and reinforced cases at $\delta = 0.6\,B; R$. The strains are given by the final Gauss point strains, but are plotted at the original Gauss point co-ordinates with the initial positions of the footing and the fill-clay boundary indicated.

The strains are found to be extremely large in a small area directly beneath the footing edge ($\approx 100\%$) and are moderately greater in the axisymmetric analyses compared to the plane strain. The reinforcing effect of reduced horizontal strains at the fill base is clearly seen by comparing the unreinforced and reinforced contour plots, i.e. the restraint mechanism.

6.5.4 Vertical and Shear Stresses in the Fill

Plates 6.3 and 6.4, Appendix 6B, depict contour plots of the vertical stresses through the fill layer normalised by the plane strain clay shear strength ($s_u^{PS} = 30\ kPa$) at $\delta = 0.6\,B; R$ for

the plane strain and axisymmetric analyses respectively. Similarly, Plates 6.5 and 6.6 show the distributions of shear stress for the plane strain and axisymmetric analyses. The stresses are given by the final Gauss point stresses and plotted at the original Gauss point co-ordinates.

The vertical stress plots clearly show the load spread beneath the footing and the concentration of higher vertical stresses to the outside edge of that load spread. There is also a noticeable reduction in the vertical stress across the reinforcement. The shear stresses at the fill base for the unreinforced and reinforced analyses are inward acting at the centre-line and become outward acting towards the edge of the vertical load spread, whereas, at the top of the fill directly underneath the footing, the shear stresses are purely outward acting (see Section 6.5.7). For the reinforced case the magnitude of the shear stresses is significantly larger, due to the membrane restraining the fill from moving outwards, and the arching effect described in Section 6.5.5 is visible. The magnitude of both the vertical and shear stresses are slightly higher for axisymmetry compared to plane strain.

The stresses along the fill base are the same as those given by the interface elements in Figures 6.20, although any minor discrepancy is due to the fact that the continuum element Gauss points are slightly removed from the interface element Gauss points.

6.5.5 Principal Stress Directions in the Fill

From the final horizontal, vertical and shear stresses at each Gauss point (at $\delta = 0.6\,B\,;\,R$) the principal stress directions in the fill layer are plotted in Figures 6.25 a) and b), Appendix 6B, at the final Gauss point co-ordinates for the plane strain and axisymmetric analyses respectively.

In the unreinforced analyses the principal stress directions in the fill layer are predominantly vertical directly under the footing and horizontal outside of the load spread. For the reinforced analyses, however, the fill layer appears to be subjected to an arching effect beneath the footing where the upper half of the fill layer is subjected to higher horizontal than vertical stresses, whereas the lower half of the fill sustains predominantly vertical stresses. A similar effect was detected in some of the embankments analysed by Kwok (1987).

6.5.6 Mobilised Friction Angle and Yield Area

The mobilised friction angle, ϕ', of the fill can be calculated from the actual stresses acting at each Gauss point by equation (6.5):-

$$\sin\phi' = \frac{(\sigma_x^2 - 2\sigma_x\sigma_y + \sigma_y^2 + 4\tau_{xy}^2)^{\frac{1}{2}}}{(\sigma_x + \sigma_y)} \tag{6.5}$$

Plate 6.7 a) shows the calculated absolute values of ϕ' throughout the fill for the plane strain unreinforced analysis at a footing displacement of $\delta = 0.6\,B$, while Plates 6.7 b) and c) show ϕ' for the plane strain reinforced analysis at $\delta = 0.2\,B$ and $\delta = 0.6\,B$ respectively. Similarly, the axisymmetric unreinforced and reinforced analyses at $\delta = 0.6\,R$ only, are illustrated in Plates 6.8 a) and b) respectively. The vertical dimension in Plates 6.7 and 6.8 is scaled by a factor of 5 for the sake of clarity.

The fill material possesses a peak plane strain friction angle of $\phi_{PS} = 40°$ and from Plate 6.7 b) it is clear that the majority of the material in plane strain conditions has reached a state of yield at a footing displacement of only $\delta = 0.2\,B$, which is why Figure 6.5 shows the entire fill layer to have yielded. In contrast the area of yield for the axisymmetric analyses, Figure 6.26, is much smaller and less of the fill material has yielded.

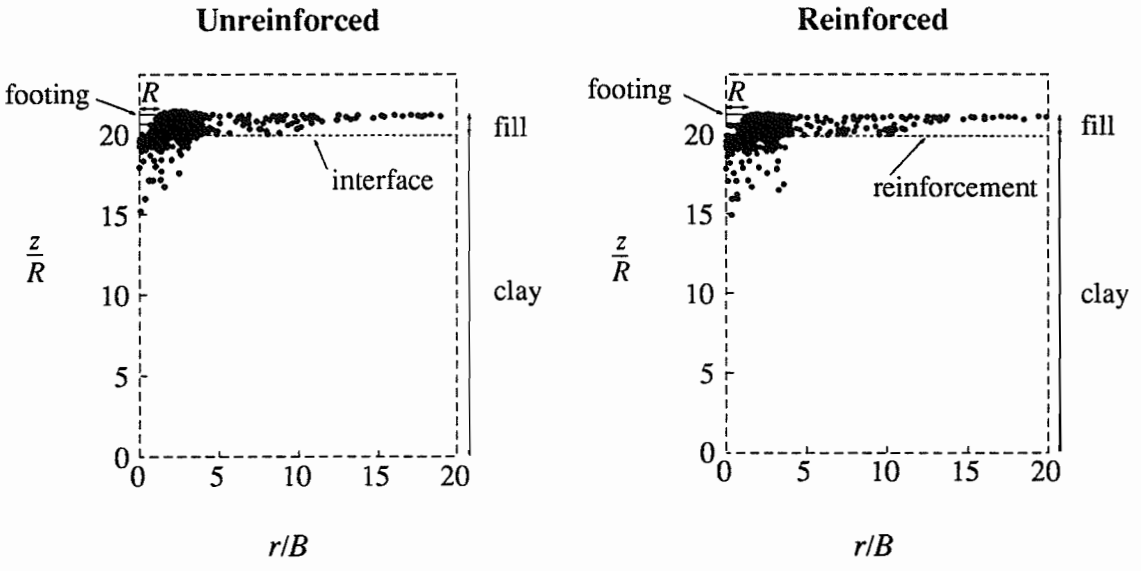

Figure 6.26: Yielded Gauss Points for the Axisymmetric Runs at $\delta = 0.6\,R$

By comparing the principal stress directions in Figure 6.25 a) and ϕ' in Plates 6.7 it is clear that for plane strain conditions all of the fill is in a state of passive failure outside of the load spread area for the unreinforced and reinforced cases. Whereas, beneath the footing ϕ' is less than ϕ of the soil and therefore the horizontal stress is greater than active conditions, particularly for the unreinforced case. This higher horizontal stress increases the tension in the reinforcement, which is partly why Houlsby *et al.* (1989) underestimates F_r (Figure 6.21). For axisymmetric conditions however, Figure 6.25 b) and Plates 6.8, a large proportion of the fill material has not yielded, particularly in the areas furthest from and directly beneath the footing. This demonstrates that the assumption in Houlsby *et al.* (1989) and Houlsby and Jewell (1990) of passive failure conditions immediately beyond the footing is correct, but that the assumed active failure conditions under the footing is inaccurate.

6.5.7 Stress Distributions on the Underside of the Footing

The distributions of the normal (σ) and shear (τ) stresses on the underside of the footing, for the unreinforced and reinforced analyses, are extracted from the continuum element Gauss points using Method 4, as described in Section 5.2 (two nearest Gauss points for plane strain and five nearest for axisymmetry), and plotted in Figures 6.27 a) and b) for the plane strain and axisymmetric analyses respectively.

The shear stresses shown in Figures 6.27 a) and b) are mostly outward acting stresses, which contradict the assumption made in Houlsby *et al.* (1989) and Houlsby and Jewell (1990) of inward acting footing shear forces. The small inward acting shear stresses at the footing edge, in the plane strain and axisymmetric analyses, are likely to be the results of discretization errors.

The integral of the Gauss point stress distributions gives the shear and normal forces per unit area acting at the footing-fill boundary. This normal force is consistent with the final nodal footing pressures, P_f for the runs shown in Figure 6.19. Clearly the normal and shear forces are larger for the reinforced analyses than for the corresponding unreinforced and furthermore in axisymmetry the normal forces are greater than in plane strain.

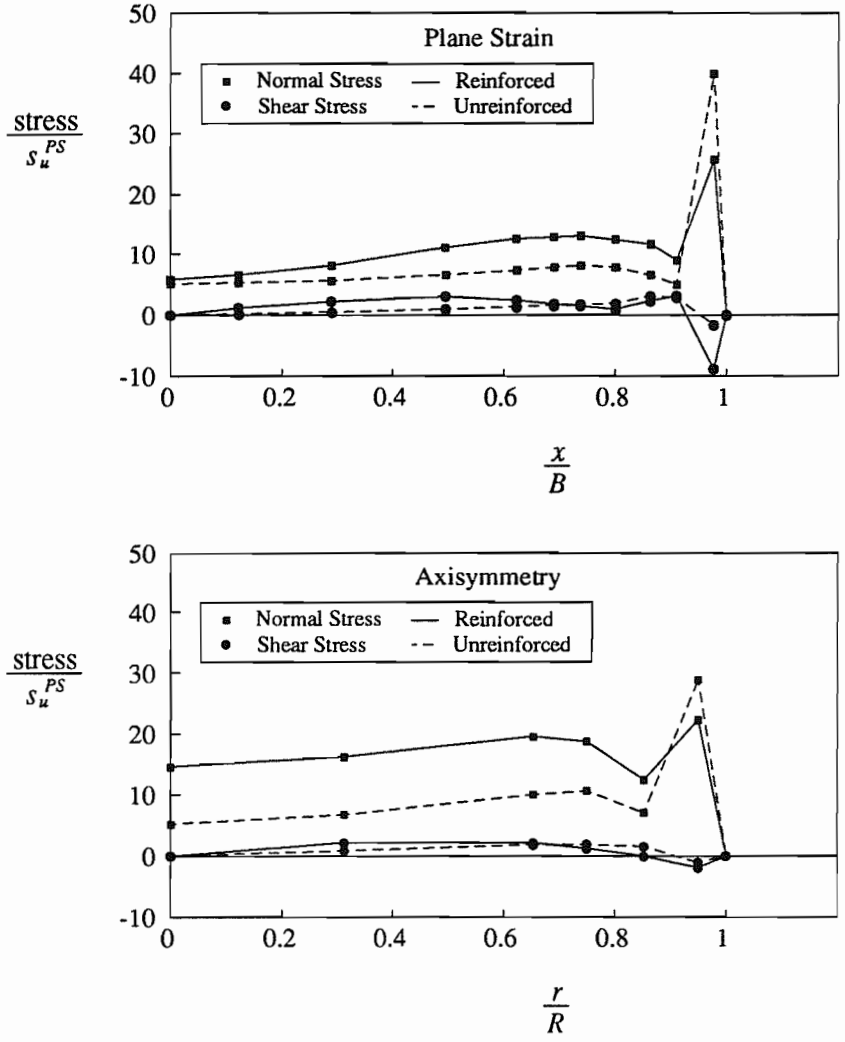

a) Plane Strain and b) Axisymmetry

Figure 6.27: Normal and Shear Stresses along underside of Footing at $\delta = 0.6\,B\,;R$

An angle of friction at the footing base, δ_f, can be established from equation (6.6):-

$$\delta_f = \tan^{-1}\frac{\tau_f}{P_f} \tag{6.6}$$

where τ_f is the total shear force per unit area at the footing base and P_f is the total normal footing pressure.

A value of δ_f is calculated for each finite element run and used in the relevant analytical computations, maintaining the convention that a negative sign indicates an outward acting footing frictional force which is consistent with the limit equilibrium methods.

APPENDIX 6A

Material Properties of the Central Parametric Analyses

WHEEL or FOOTING		
	Perfectly Rough Contact	
B	Footing Half Width for Plane Strain	0.25 m
R	Footing Radius for Axisymmetry	0.25 m
δ	Rut Depth	0.15 m
FILL SUBBASE		
G_f	Shear Modulus	6000 kPa
ν_f	Poisson's Ratio	0.2
γ_f	Bulk Unit Weight	19 kN/m^3
D_f	Fill Depth	0.3 m
ϕ_T	Triaxial Friction Angle	35.6 °
ϕ_{PS}	Plane Strain Friction Angle	40 °
γ_a	Degree-of-Association	0.6
ψ_{PS}	Plane Strain Dilation Angle	24 °
CLAY SUBGRADE		
G_c	Shear Modulus	1600 kPa
ν_c	Poisson's Ratio	0.49
γ_c	Bulk Unit Weight	19 kN/m^3
D_c	Clay Depth	5 m
s_u^T	Undrained Triaxial Shear Strength	26 kPa
s_u^{PS}	Undrained Plane Strain Shear Strength	30 kPa
REINFORCEMENT MEMBRANE		
J	Reinforcement Stiffness	300 kN/m
L	Reinforcement Length	5 m
ν_r	Poisson's Ratio	0
t_0	Initial Thickness	*unity*
K	Reinforcement Bulk Modulus	$K = J\frac{t_0}{(1-\nu_r^2)} = 300\ kN/m$
INTERFACE PROPERTIES		
k_s	Shear Interface Stiffness	100 000 kN/m
k_n	Normal Interface Stiffness	200 000 kN/m
ϕ_i	Friction Angle	35 °
ψ_i	Dilation Angle	10 °

APPENDIX 6B

Contours and Trajectories of the Central Parametric Analyses

Plane Strain

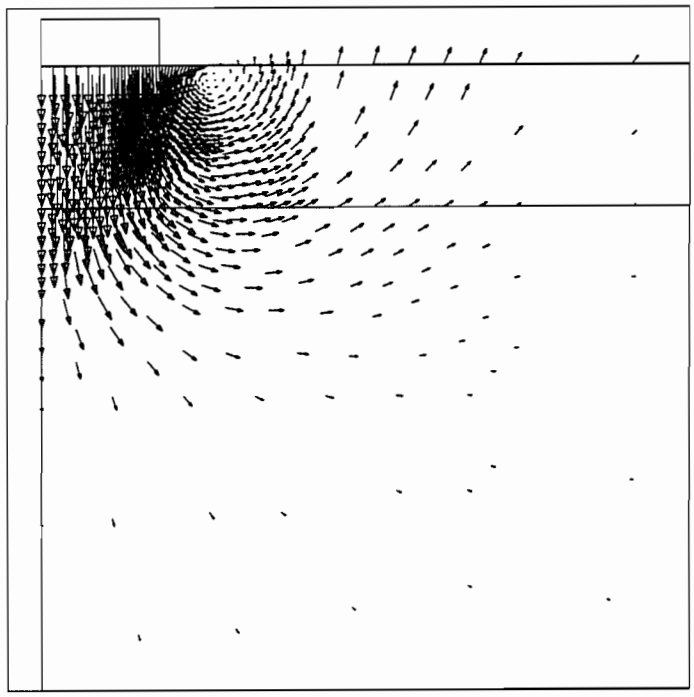

Unreinforced

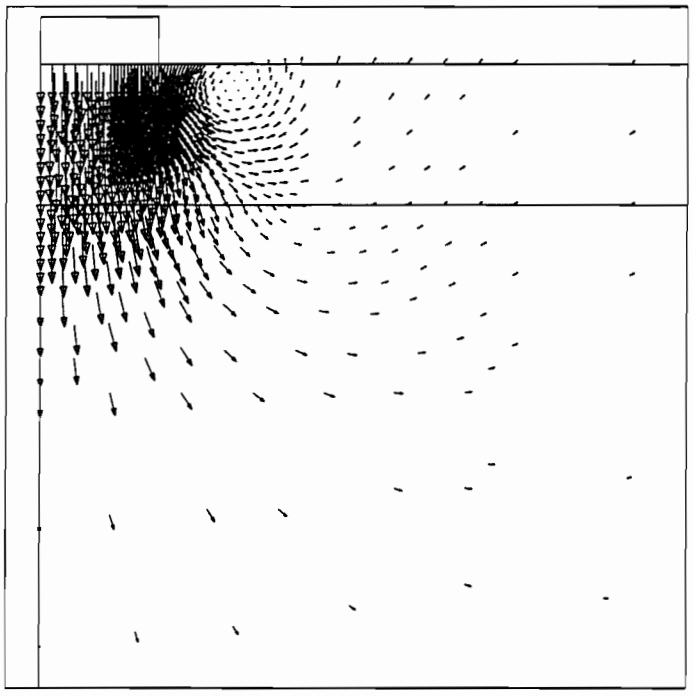

Reinforced

Figure 6.24 a): Nodal Displacement Vectors in Plane Strain

Axisymmetry

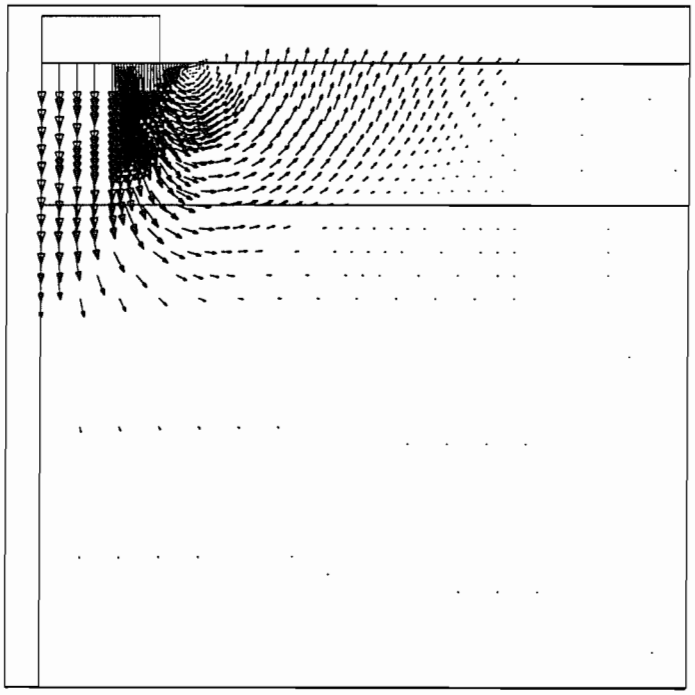

Unreinforced

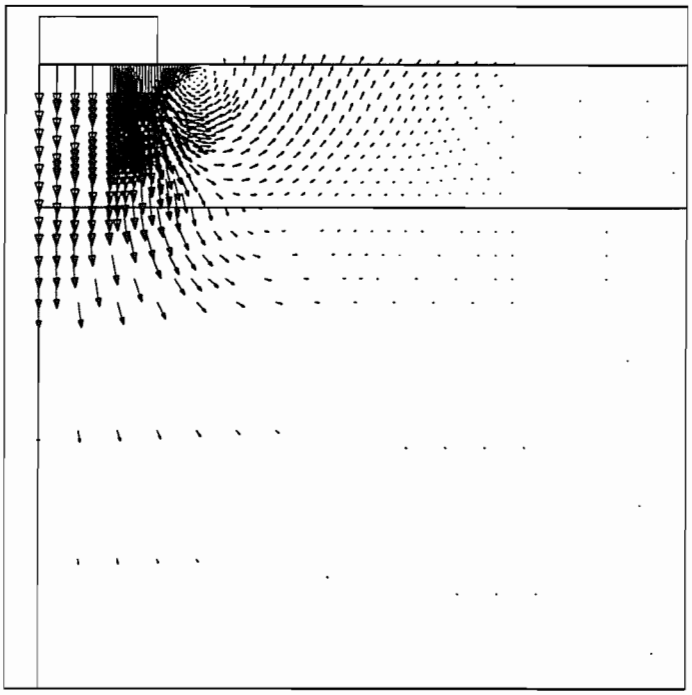

Reinforced

Figure 6.24 b): Nodal Displacement Vectors in Axisymmetry

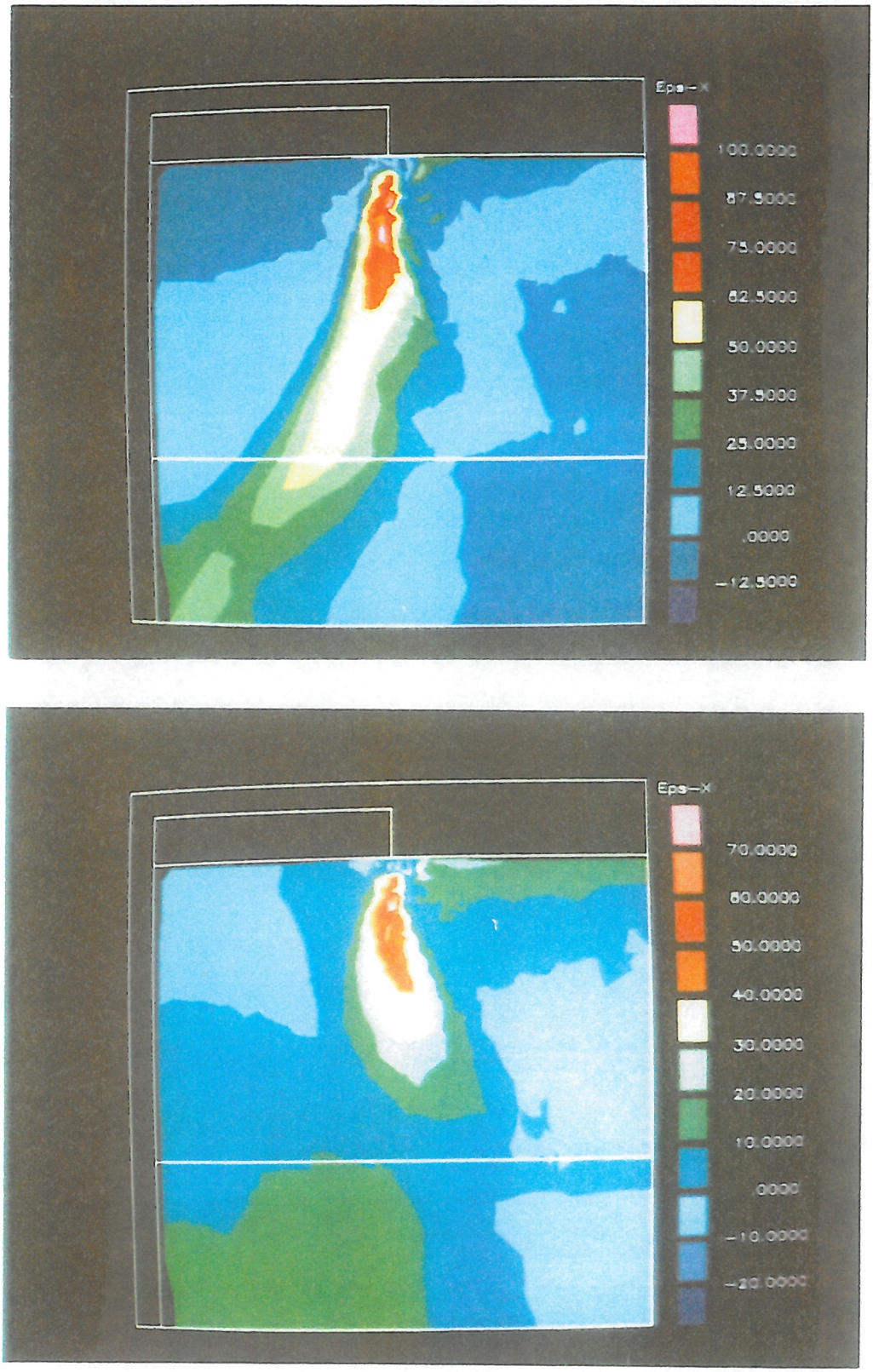

a) Unreinforced and b) Reinforced

Plate 6.1: Horizontal Strains (Eps-X %) in Plane Strain at $\delta = 0.6\ B$

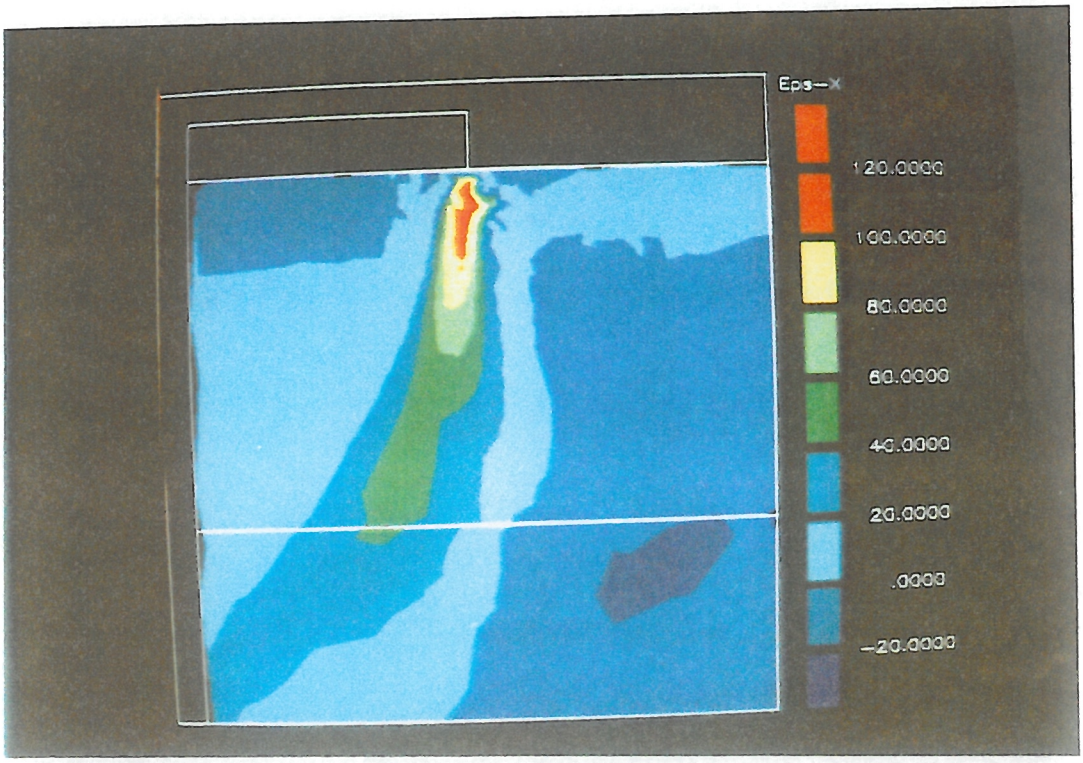

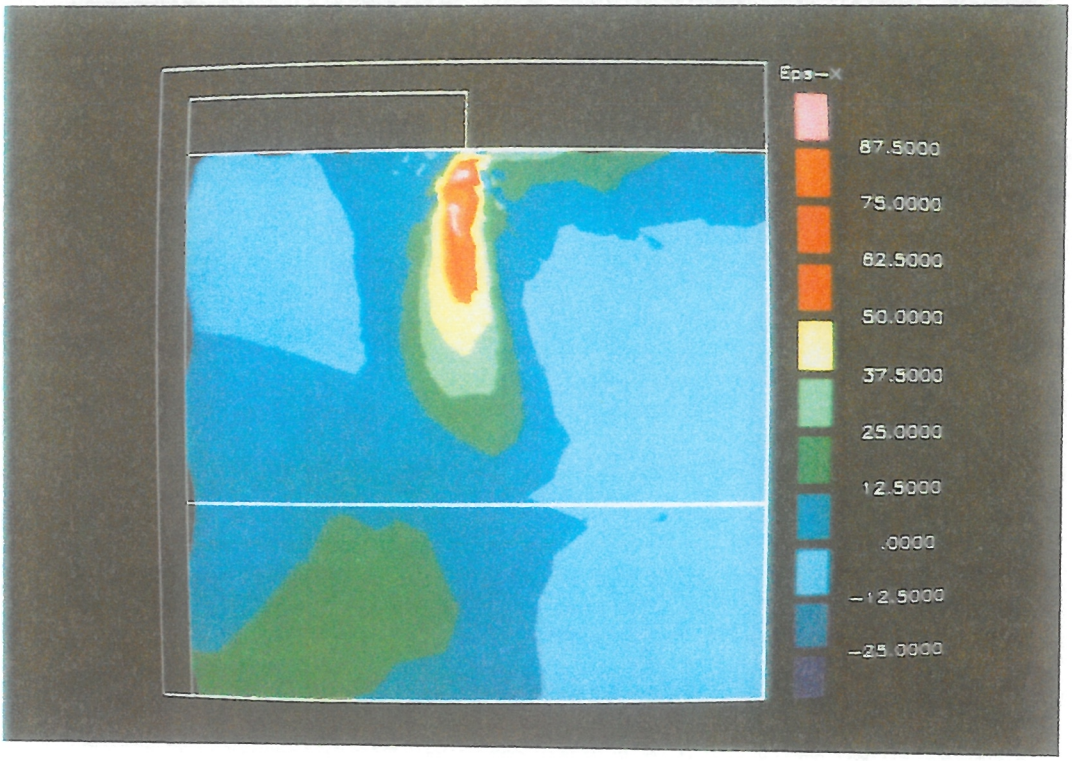

a) Unreinforced and b) Reinforced

Plate 6.2: Horizontal Strains (Eps-X %) in Axisymmetry at $\delta = 0.6\ R$

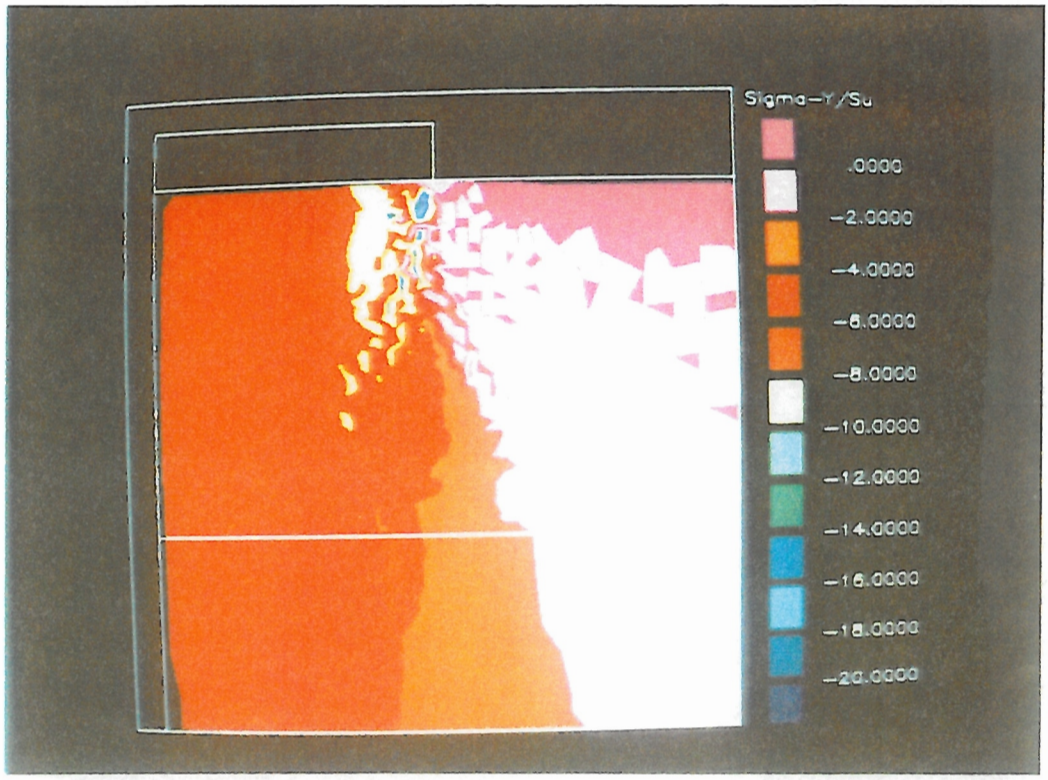

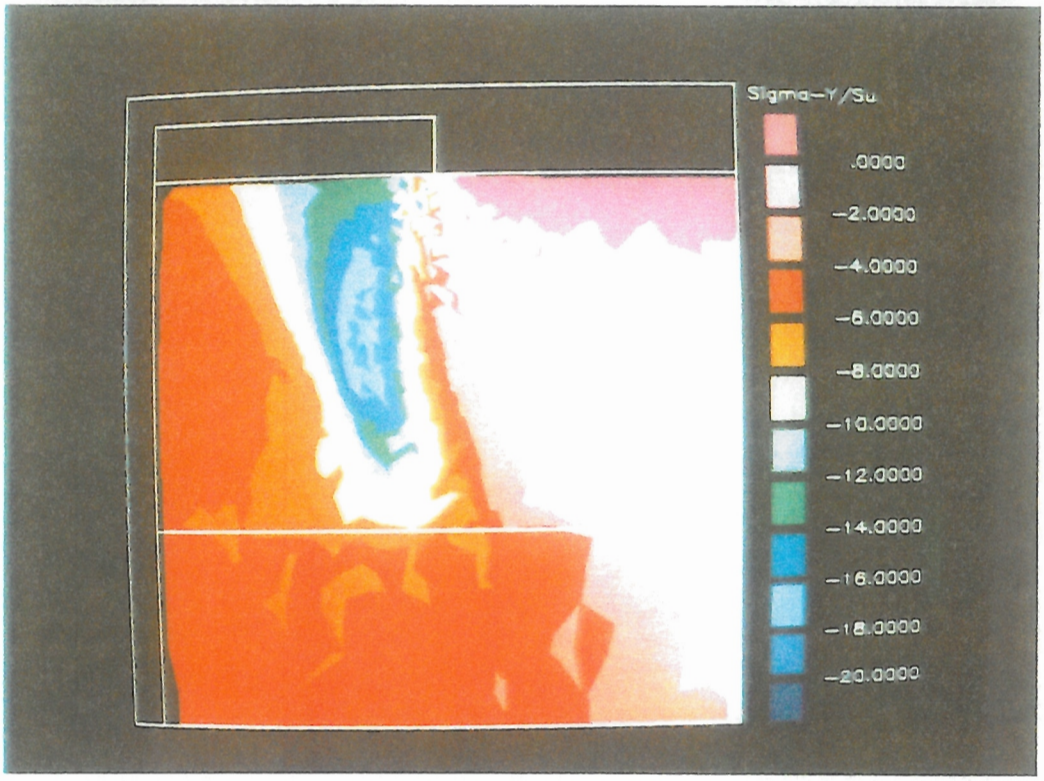

a) Unreinforced and b) Reinforced

Plate 6.3: Vertical Stresses (Sigma-Y/Su) in Plane Strain at $\delta = 0.6\ B$

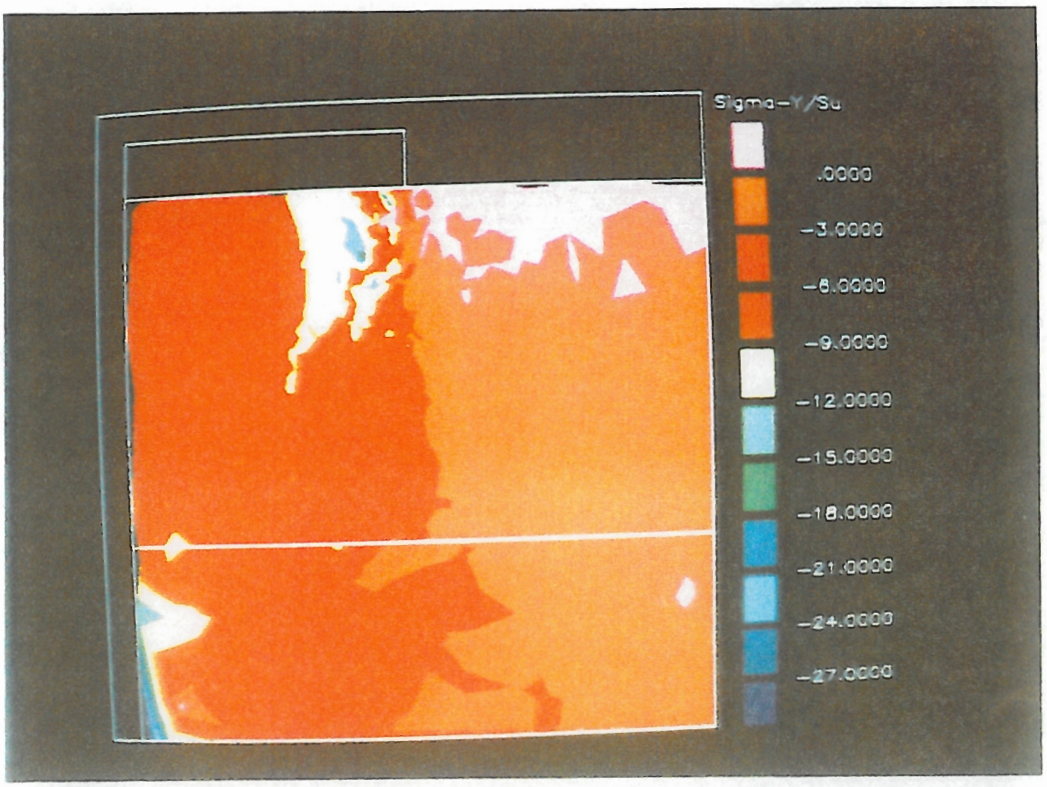

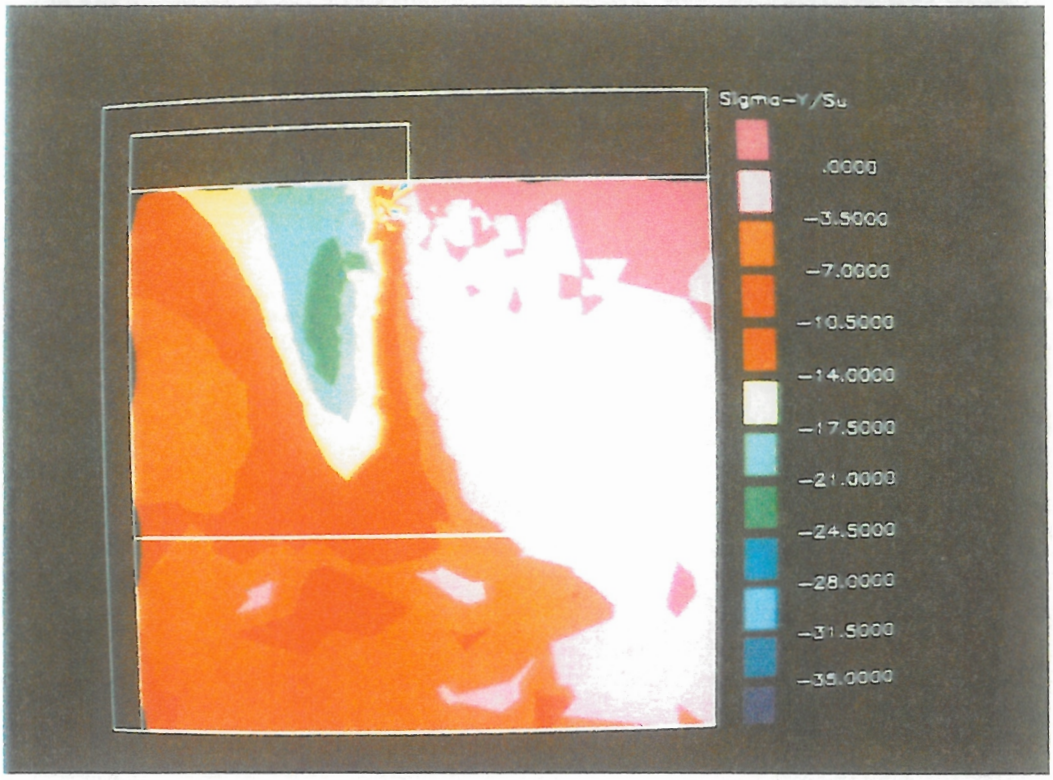

a) Unreinforced and b) Reinforced

Plate 6.4: Vertical Stresses (Sigma-Y/Su) in Axisymmetry at $\delta = 0.6\,R$

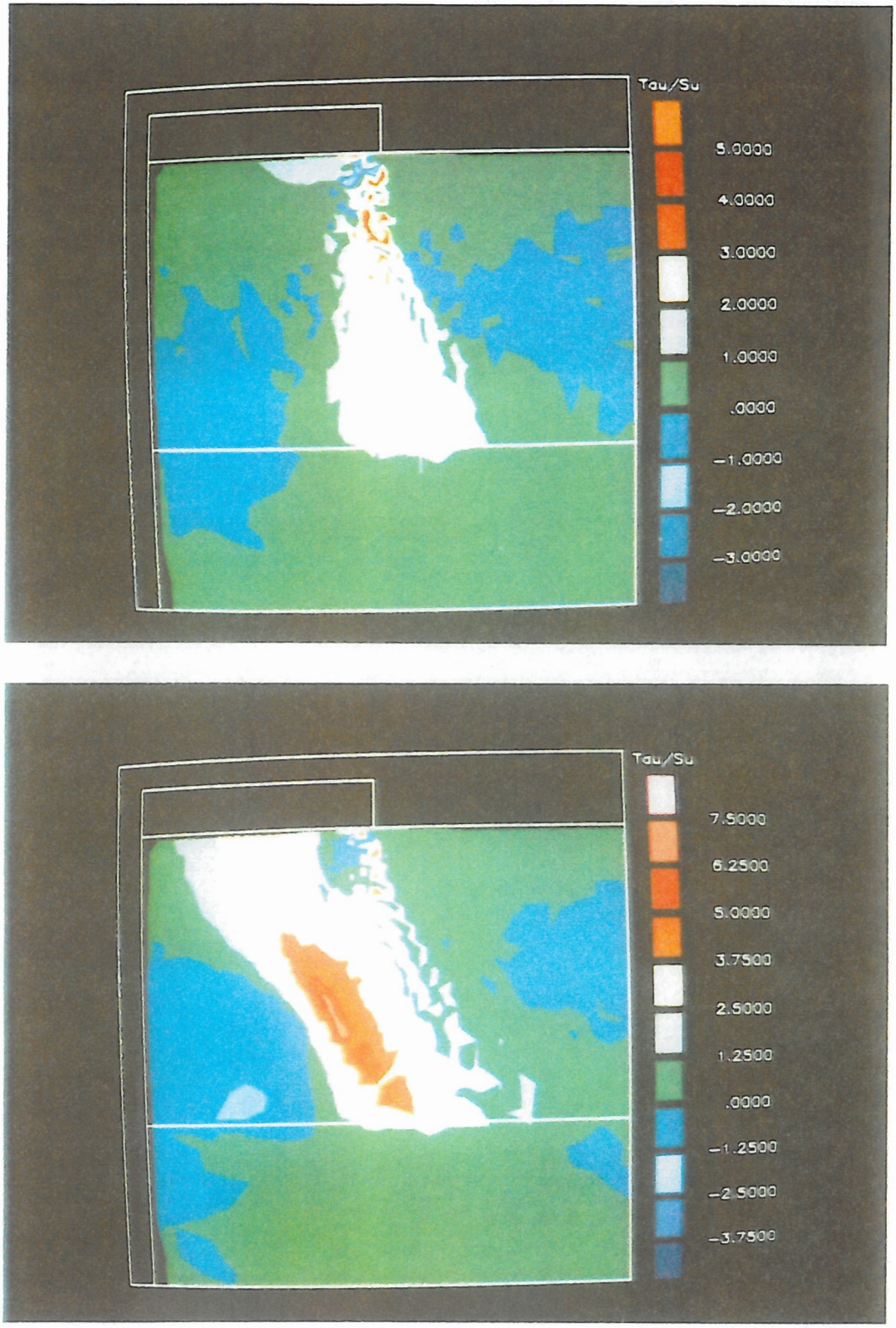

a) Unreinforced and b) Reinforced

Plate 6.5: Shear Stresses (Tau/Su) in Plane Strain at $\delta = 0.6\ B$

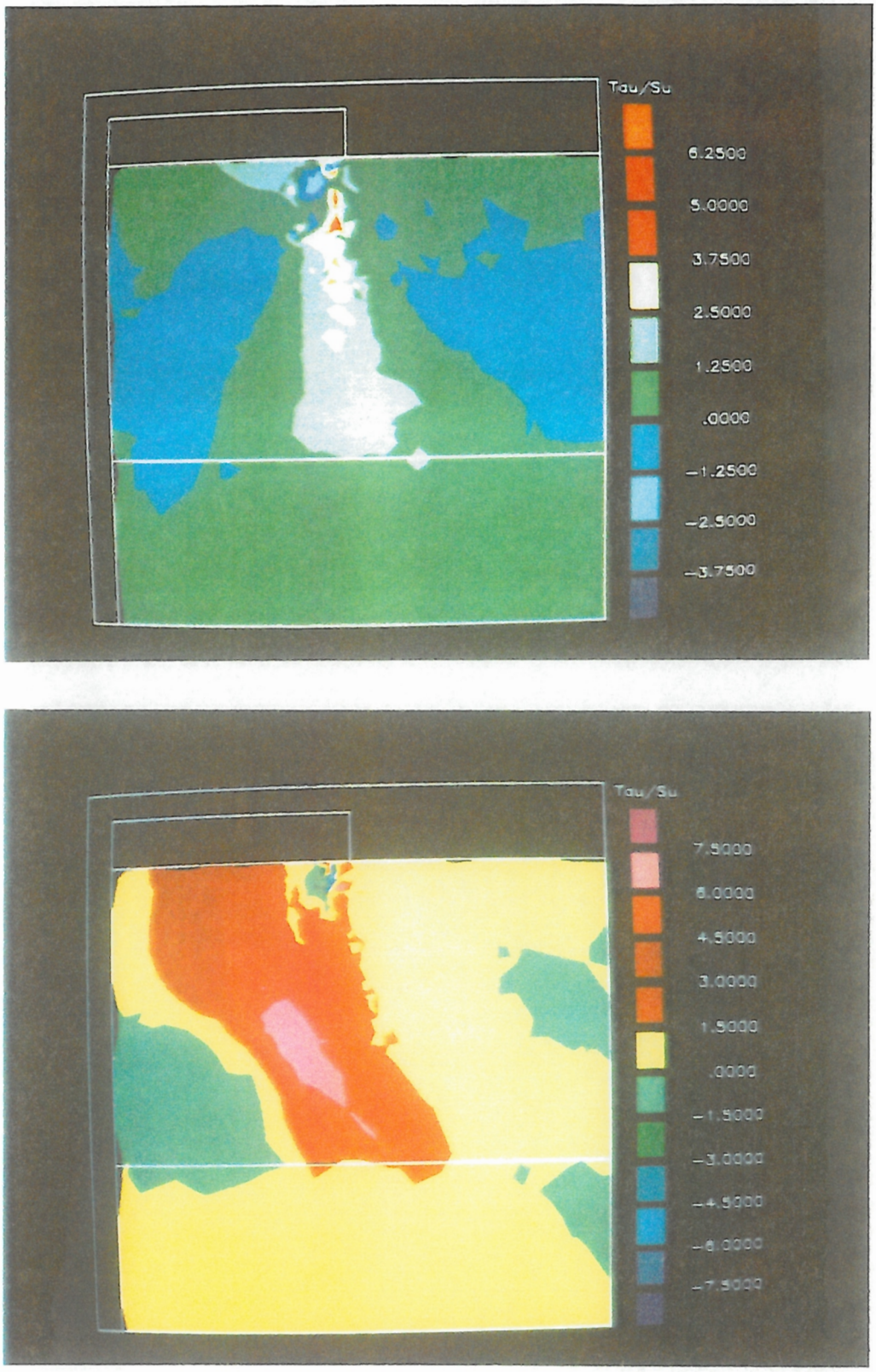

a) Unreinforced and b) Reinforced

Plate 6.6: Shear Stresses (Tau/Su) in Axisymmetry at $\delta = 0.6\,R$

Plane Strain

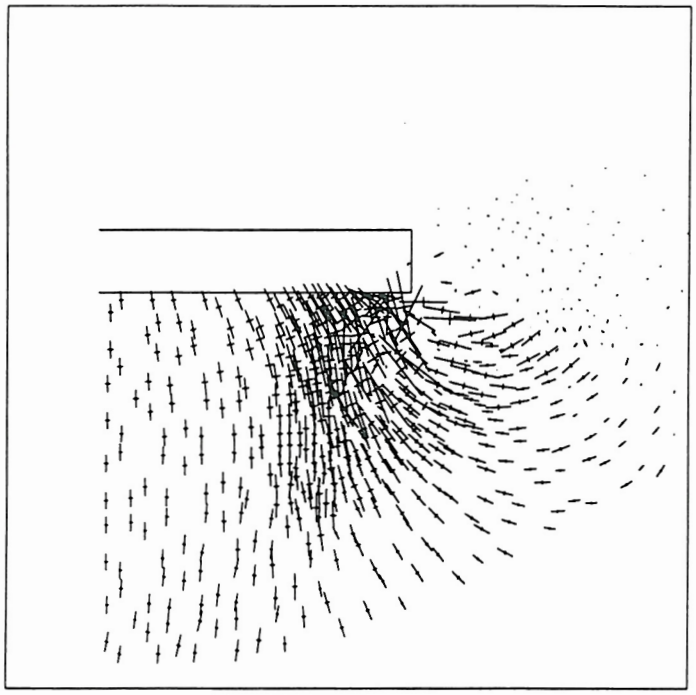

Unreinforced

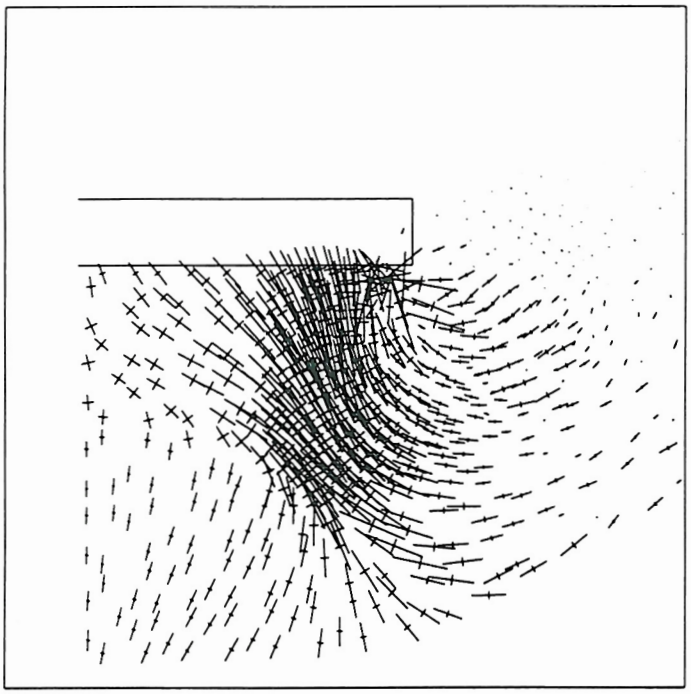

Reinforced

Figure 6.25 a): Plane Strain Principal Stress Directions in the Fill at $\delta = 0.6\,B$

Axisymmetry

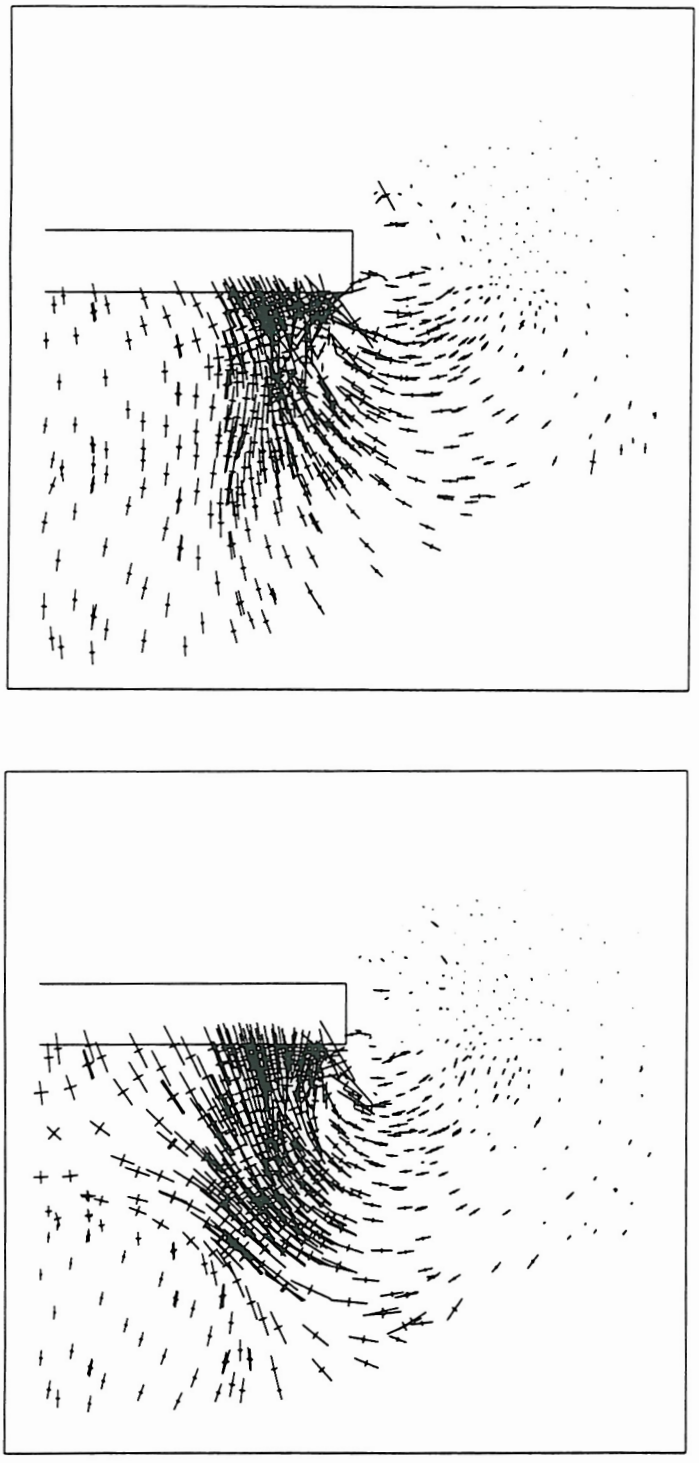

Unreinforced

Reinforced

Figure 6.25 b): Axisymmetric Principal Stress Directions in the Fill at $\delta = 0.6\,R$

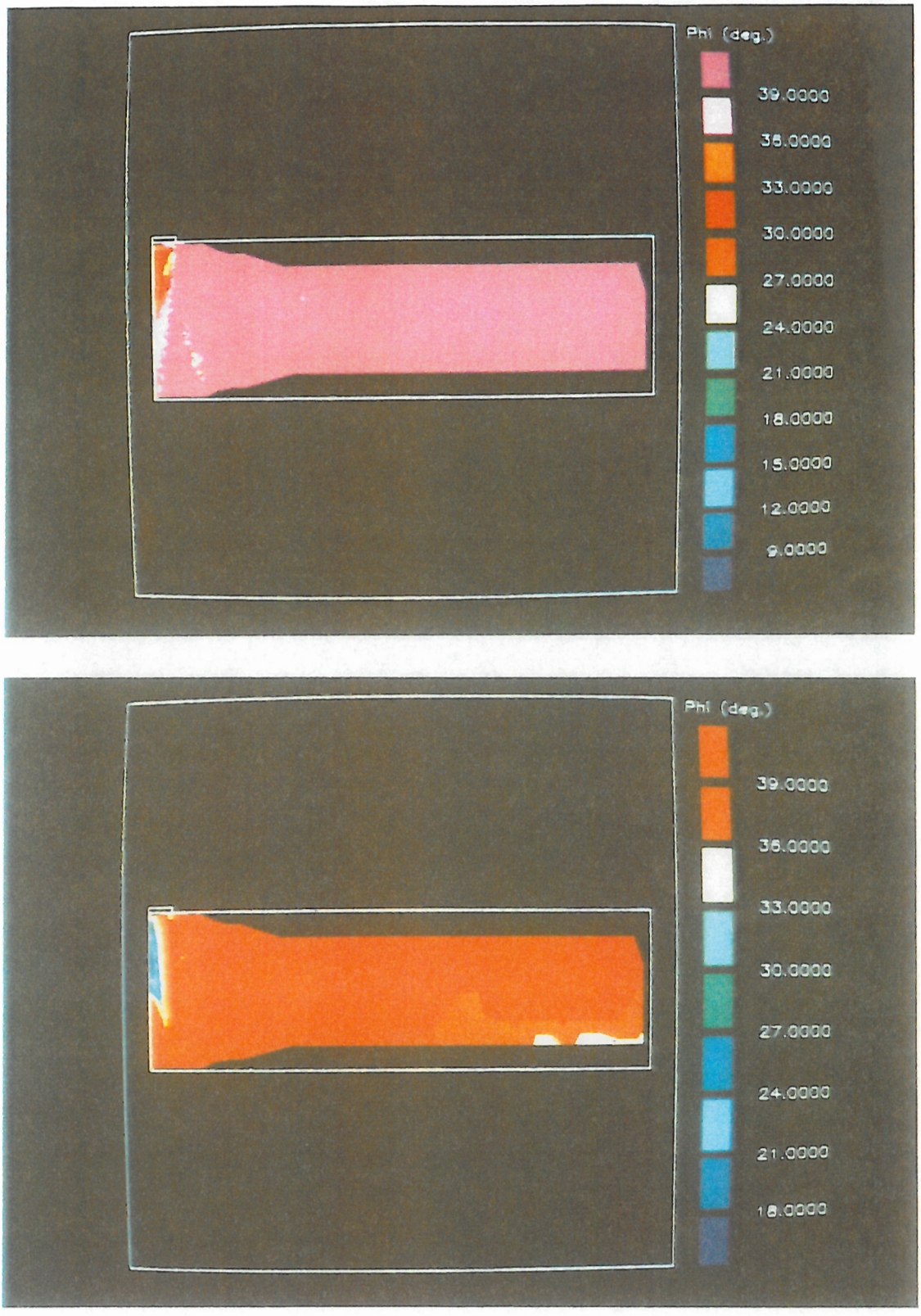

a) Unreinforced at $\delta = 0.6\,B$ and b) Reinforced at $\delta = 0.2\,B$

Plate 6.7: Mobilised Angles of Friction (ϕ') in Plane Strain

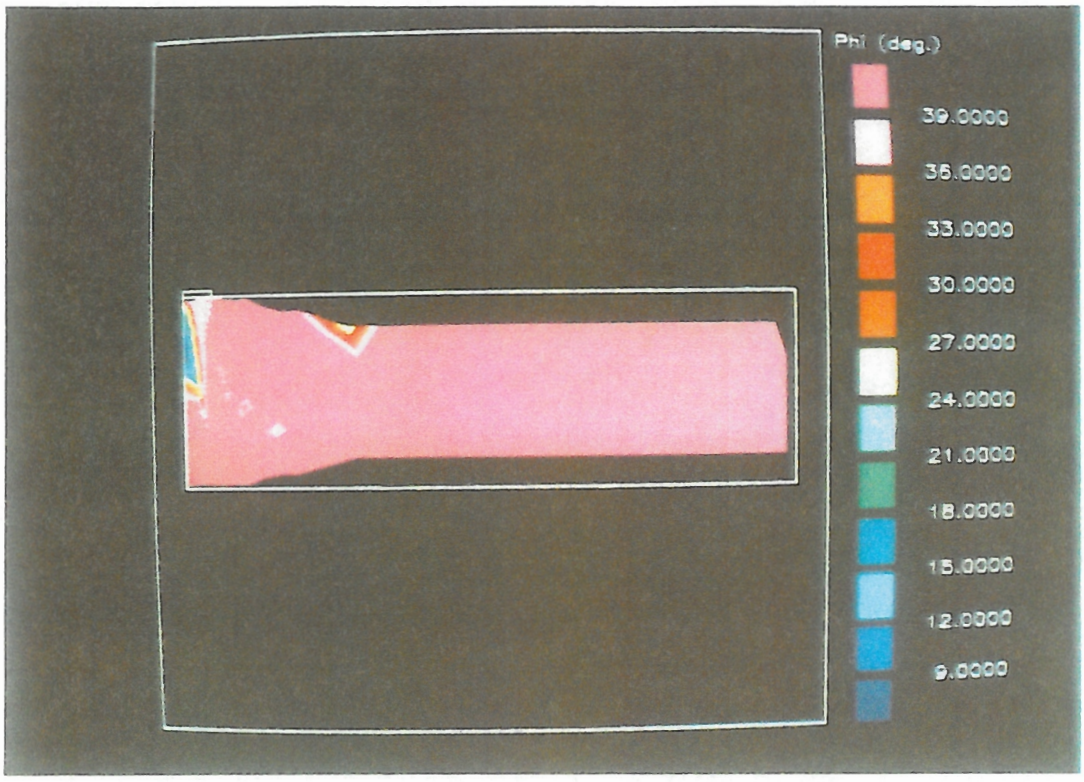

c) Reinforced at $\delta = 0.6\,B$

Plate 6.7: Mobilised Angles of Friction (ϕ') in Plane Strain

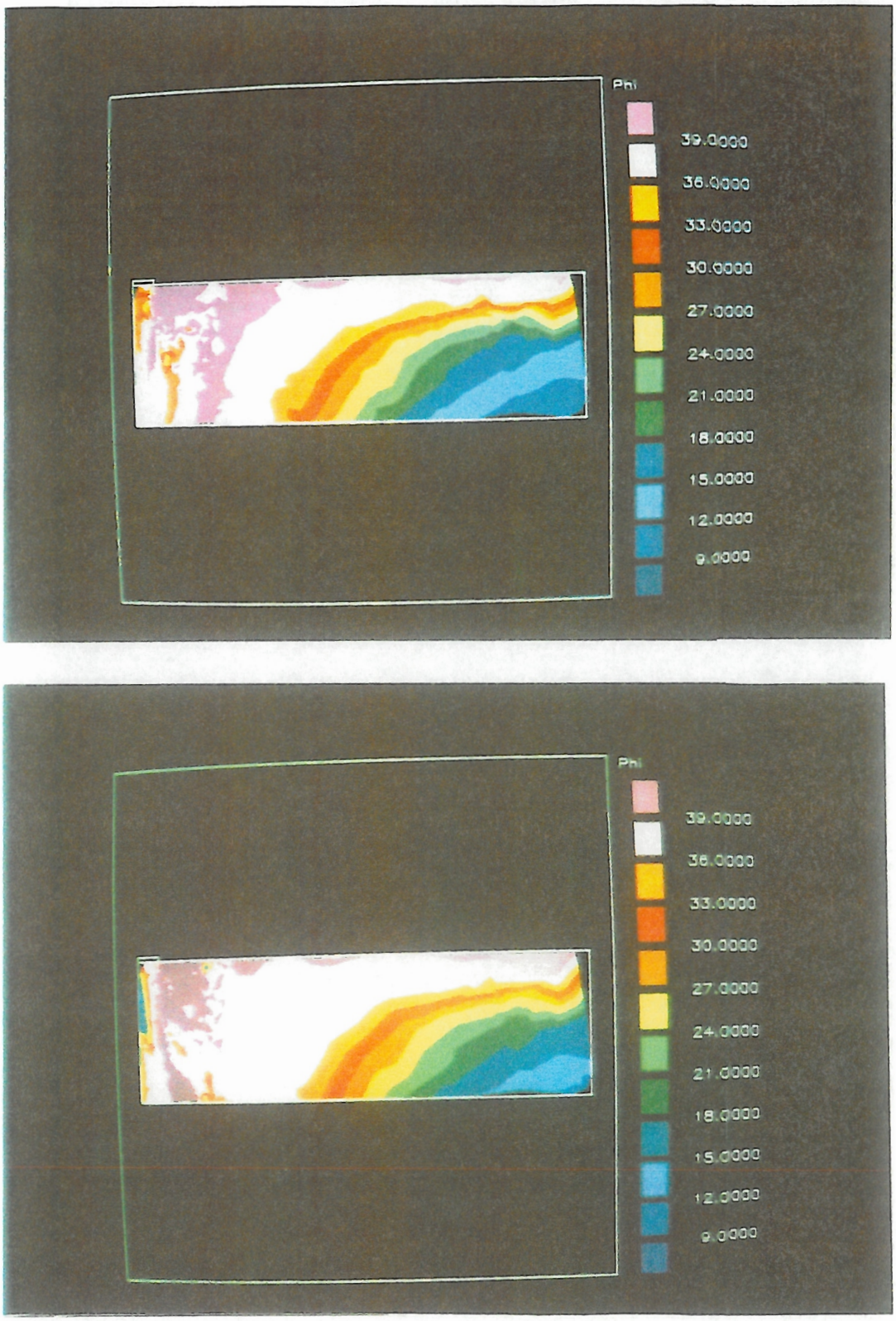

a) Unreinforced and b) Reinforced

Plate 6.8: Mobilised Angles of Friction (ϕ') in Axisymmetry at $\delta = 0.6\,R$